## Opto-Electronics Review

# A review of the current state-of-the-art in Fano resonance-based plasmonic metal-insulator-metal waveguides for sensing applications

R. Adhikari[a,b], D. Chauhan[a], G. T. Mola[c], R. P. Dwivedi[a*]

[a] Faculty of Engineering and Technology, Shoolini University, Bajhol, (HP) 173229, India
[b] School of Engineering, Pokhara University, Pokhara Metropolitan City 30, Kaski, Nepal
[c] School of Chemistry and Physics, University of Kwazulu Natal, Scottsville, South Africa

| Article info | Abstract |
|---|---|
| | Fano resonance is an optical effect that emerges from the coherent coupling and interference (constructive and destructive) between the continuous state (background process) and the Lorentzian state (resonant process) in the plasmonic waveguide-resonator system. This effect has been used in the applications like optical sensors. These sensors are extensively used in sensing biochemicals and gases by the measurement of refractive index changes as they offer high sensitivity and ultra-high figure of merit. Herein, we surveyed several plasmonic Fano sensors with different geometries composed of metal-insulator-metal waveguide(s). First, the resonators are categorized based on different architectures. The materials and methods adopted for these designs are precisely surveyed and presented. The performances are compared depending upon the characterization parameters like sensitivity and figure of merit. Finally, based on the survey of very recent models, the advances and challenges of refractive index sensing deployed on Fano resonances are discussed. |

## 1. Introduction

Plasmon propagation is a phenomenon that occurs at the interface of metal-dielectric due to the interplay of light with metal structures at optical spectra which has facilitated the achievement of highly complex nano-sized devices by controlling and manipulating light on a nanometric scale [1]. This occurs within the plasmonic waveguides at the metal-insulator interface when they are excited by electromagnetic (EM) waves. Thus, the coupled state of the incident EM waves (photons) and free surface electrons of the metal resulted in other waves called surface plasmon polaritons (SPPs). SPPs are the EM signal transmitted at the metal-insulator alliance that decays significantly along the interface [2]. Plasmonic waveguides (WG) use SPPs to carry data across themselves [3]. SPP-based plasmonic WGs offer the capability of confining the light in the submicron region by breaking the diffraction limit and they increase the local EM field strength by many orders of magnitude [4]. These are the points behind their extensive applications in integrated photonic devices and circuits [5]. Moreover, SPPs-based resonance sensors possess high sensitivity for label-free detection and refractive index sensing [6]. Thus, they have been explored much through experiments and theoretical methods. Since SPPs are much dependent on the architecture of WG, material properties, refractive index (RI) variations of the surrounding and transmission condition of the incident light, the sensors based on SPPs are tuned by these properties, and, therefore, show high sensitivity ($S$) for RI dependent sensors [7].

Several SPP-based optical WG configurations ensure the two mail characteristics (propagation length and modal confinement) of the WGs which are important for optical integrated devices. Metal-insulator-metal (MIM), insulator-metal-insulator (IMI), dielectric-loaded surface plasmon polariton (DLSPP), gap plasmon polariton (GPP), channel plasmon polariton (CPP), and hybrid plasmon

polariton (HPP) are the popular WG structures presented in the literature [8,9]. Among these configurations, MIM is abundantly explored and implemented since it possesses many advantages such as near-zero bend loss, deep subwavelength confinement of EM waves, longer propagation length, simple design, and wider operating frequency ranges [10]. Such features of the MIM are used in sensing applications [11]. In addition to these features, MIM WGs have other prominent features like small device size, possibility of high-density integration, and easy manufacturing process [12] which make them appropriate for many other optical applications such as filters, switches, logic gates, splitters, demultiplexers, perfect plasmonic absorbers, modulators, and sensors [11]. MIM WGs are also suited for integration with photonic circuits as they convey a proper balance between bend losses and light confinement.

In the MIM WG system, in case of sensing applications, the resonance condition should be considered. Resonance is an enhancement of the system response to an external excitation at a particular wavelength referred to as a resonant wavelength of the system. The resonance(s) may be characterized by a symmetrical profile of single/multiple peak/dip(s) as described by the Lorentzian function (Lorentzian resonance) or by asymmetric profile. The latter profile is achieved by mixing of discrete state response and continuum state response of the system, and the corresponding excitation is referred to as Fano resonance (FR). The pictorial demonstration of FR is shown in Fig. 1.
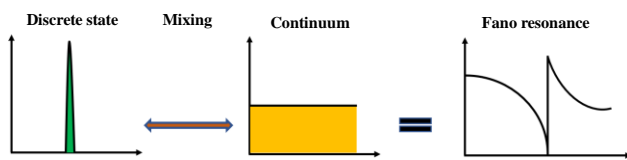


**Fig. 1.** Conceptual illustration of the FR generation [13].

FR is described by the Fano formula as [13]:

$$Y = \frac{(q + X)^2}{1 + X^2},\qquad(1)$$

where the Fano parameter $q$ is the cot function of the continuum phase shift ($\delta$) between two modes and $X$ denotes the standard parameter giving the position and width of the resonance. Factors such as material characteristics and system geometry influence this shift. Moreover, the phase shift is governed by erosion, fabrication errors, change of ambient refractive index (RI), and so on. Thus, its asymmetric nature is shown. From the above, it is observed that the Fano parameter is influenced by the RI change, which is the foundation for RI sensing applications. Therefore, the interference between a spectrally overlapping broad resonance or continuum and a narrow discrete resonance is the primary condition for an FR. Tunable coupled plasmonic structures constructed of standard plasmonic materials like silver (Ag) or gold (Au) can meet these requirements [14]. This optical behaviour of FR found in MIM-based structures is interesting. Plasmonic FRs are more important than the Lorentzian resonances because they offer exotic characteristics like

sharply asymmetric line shape [15], ultra-low radiation damping [16], high spectral sensitivity to changes in the local dielectric environment [17], and large induced field enhancement. The ultra-low radiation damping feature at a Fano dip/peak is responsible for a very narrow resonance linewidth which ultimately increases the sensor figure of merit and detection resolution.

This review describes plasmonic RI sensors by combining the advantages of SPPs, MIM, and FRs into a single device. Plasmonic RI sensors based on FR have potential implementations in the fields of human and biomedical sciences, agriculture and environmental sciences, as well as in food technology. For instance, with RI sensors, the pH concentration of a given solution/soil can be determined, as well as the variability of organic chemicals in the human body due to some abnormalities. The concentration of some gases in the environment based on the variability of RIs can be determined, as well. The working mechanism of such sensors is based on the light-matter interaction. The interaction can be described based on the MIM WG cross-section shown in Fig. 2. When the light is incident on the WG from one end, it excites the medium of the core, thus producing an EM field that comprises propagating surface plasmons (SPs) highly concentrated at the metal surface as shown in Fig. 2(a). When a substance under examining (SUE) is filled in the core by replacing the previous medium, the effective refractive index ($n_{\mathrm{eff}}$) of the sensor varies, and subsequently, the resonance wavelength ($\lambda_{\mathrm{res}}$) experiences a redshift as demonstrated in Fig. 2(b). This is because differences in the RI of the surrounding surface have a significant impact on SPs. SP propagation and resonances are affected not only by the medium RI, but also by the medium polarization, particle size, shape, and surface chemistry, as well as metal nature. However, the effects of change in RI ($\Delta$RI) can be quantified by evaluating the changing effects in one of the attributes of light associated with the SPs, for instance, switches in the $\lambda_{res}$, intensity, or phase [18]. Herein, this paper focus only on changes in the $\lambda_{res}$ called the wavelength interrogation method. The sensing phenomenon based on the wavelength interrogation method to determine the changes in RIs of the substances
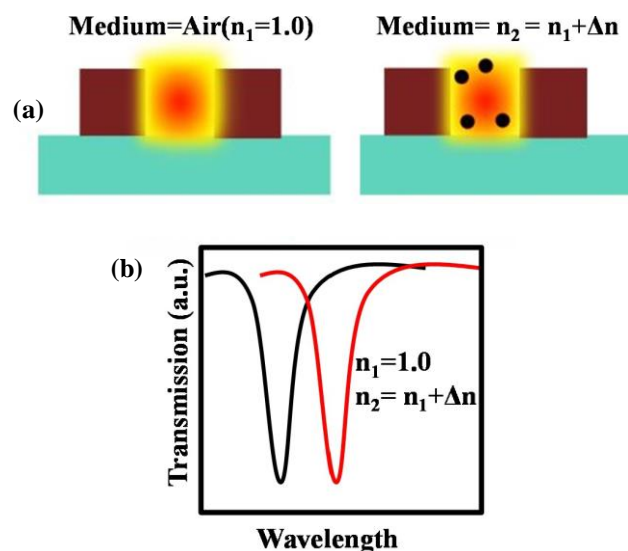


**Fig. 2.** Diagrammatic demonstration of the sensing technique (a); redshift in $\lambda_{\mathrm{res}}$ due to changes in the material medium (b) [18].

has been characterized by the spectral line shapes emerged from different configurations. These spectral lines exhibit either the Lorentzian resonance or the FR [19] depending upon the structural arrangements and others.

Many researchers have proposed the plasmonic sensors based on a WG-coupled resonator structure that enable some symmetrical Lorentzian-like profile. Some of the examples are illustrated next. Huang *et al*. demonstrated a subwavelength scale slow-light enhanced RI sensors structures consisting of double stubs and an array of stubs resonators with a figure of merit (FoM) of 10.3383 [20]. Luo *et al*. proposed an MIM WG side-linked with a double cavity (rectangular and disk cavities) which provides an $S$ of 1136 nm/RIU with an FoM of 51.275 [21]. Rakhshani *et al*. designed a racetrack resonator being coupled with MIM WG and simulated numerically to achieve an $S$ as high as 4650 nm/RIU with an FoM of 23.4 RIU$^{-1}$ (in this case FoM is obtained by dividing the sensitivity by the bandwidth of resonance [full width at half maximum (FWHM)]: FoM = $S/\Delta\lambda$FWHM) [22]. Butt *et al*. demonstrated a sensor with an MIM WG square ring resonator by simulating with a finite element method (FEM) so that the maximum $S$ obtained was of 1367 nm/RIU with an FoM of 25 [23]. Butt *et al*. proposed and investigated an MIM square ring resonator loaded with an array of silver nano-dots which achieved the maximum $S$ up to 1240 nm/RIU and the highest FoM of 20 [24]. From these results, it can be seen that $S$ can be enhanced but FoM cannot be enhanced due to their less sharp spectral Lorentzian lines. A similar conclusion was drawn by Ref. 18 where the lowest $S$ of 596 nm/RIU and the highest $S$ of 3460 nm/RIU were surveyed. These designs have incorporated the concept of incrementing the light substance interaction to improve the sensing performances ($S$, FoM, etc.). To materialize the excessive interaction, the researchers have optimized their structures by increasing the resonator quality factor (more light confinement). Various design approaches such as ring, cavity resonators with some modifications like embedding nano-walls, nano-rods, and nano-dots, etc., have been proposed to achieve resonances to obtain the sharp spectral profile, but they can only furnish slight enhancements in sensing despite their high design complexities. Moreover, the FoM achieved in such designs falls below 60 which is not enough to characterize the sensing ability. Thus, it is always possible to improve the sensing performance (RIU, $S$ and FoM) of the sensors by generating a sharp spectral profile as is achieved through FR-based configurations. This review focuses on such an important optical effect, the FR effect, that is derived from MIM WG-based structures for use in RI sensing applications. The trend and status of such sensors can be observed from the disseminated articles statistics as recorded in the Scopus database. The bar diagram that depicts the number of articles mentioning the plasmonic Fano sensor published in 2012–2020 is shown in Fig. 3.

It is seen from Fig. 3 that the Fano-based sensor using plasmonic technology has recently been the key area of research. The maximum number of articles has been published in 2019. Numerous commercially available high-performance photonic simulation tools have made this extensive research easy. For instance, by using numerical techniques such as the FEM of COMSOL multiphysics and
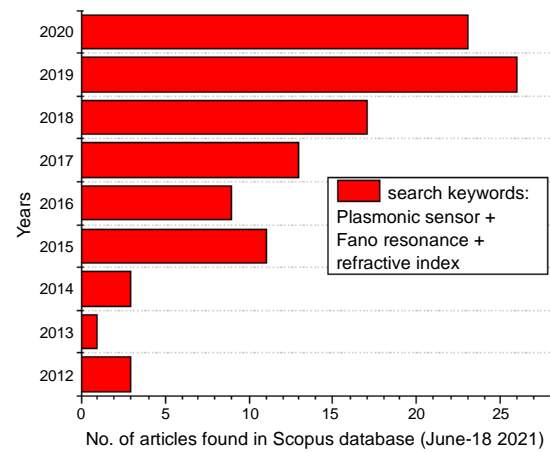


**Fig. 3.** Numbers of articles mentioning plasmonic Fano refractive index sensing [18].

the finite difference time domain (FDTD) method, the influence of structural parameters and material media variations on sensing performances and transmission spectra is investigated.

## 2. MIM waveguides and their optical effects

As shown in Fig. 4, the MIM WG consists of three layers with a dielectric layer sandwitched between two metal layers.

The metal layers act as a cladding whereas the dielectric layer acts as a core for propagating electromagnetic waves (as SPPs). The arrangement of these layers can be either horizontal or vertical, however, the horizontal version as shown in Fig. 4(a) has recently been used popularly for sensing applications because it offers a large surface area for the detection of substances. Propagating SPs inside the MIM WG are dispersive. The dispersion plot is analytically solved in Ref. 25 and demonstrated in a graphical form in Refs. 18 and 26 as presented in Fig. 4(b). It shows that the
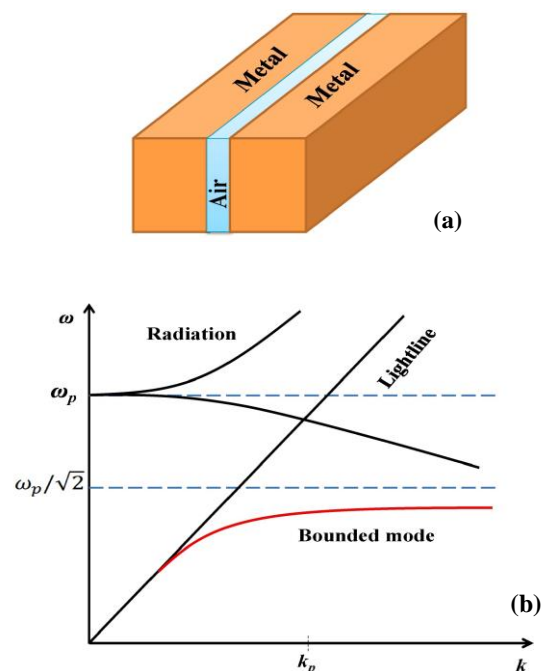


**Fig. 4.** 3-D view of the metal-insulator-metal waveguide (a) and its dispersion plot (b) [18].

bounded electromagnetic modes (the SPP modes) have remarkable features including peculiar tunability, long plasmon lifetime, and strong subwavelength confinement. Therefore, the MIM WGs are the promising nanostructures upon which many optical communication devices and optical sensors are designed and integrated into the chip level. When some light is incident in the core of the MIM waveguide, then depending on the type of coupled geometry, different optical phenomena like electromagnetically induced transparency (EIT) [27,28] and FR [29–31] can be seen. Apart from MIM WGs-based structures, FRs can be visualized in other structures, as well, and such highly explored structures mainly include rings [30], photonic crystal [32], and planar oligomers [15]. Nanostructures with optical phenomena like EIT or FRs have recently got a lot of attention, and they have been the subject of much theoretical and experimental research. Moreover, FRs generating MIM WG-based structures for RI sensing applications have grabbed the interest of many researchers because they bring the benefits of FR and MIM WG into a single unit. Inherently, FRs are highly sensitive to RI changes, structural design, and structural parameters, and MIM WG offers a good balance between the losses and modal confinement into the nano-meter range. Thus, such sensors can be an integral part of integrated optical circuits [33].

### 2.1. Fano resonance basics

Various researchers have defined FRs in different ways. According to quantum, or classical theory of physics, the FR is a basic resonant effect that emerges as an intrusion effect between a localized state and a continuum band [34]. This is a result obtained from the linking and intrusion of a non-radiative mode and a continuum of radiative EM signals which are characterized by a distinctive asymmetric line shape [14,35]. These two modes are spectrally and spatially overlapped. Similar optical effect visualized in the classical atomic system as the result of interference of a discrete auto-ionized state and a continuum state is called EIT. Both effects have similar physical mechanism but dissimilar spectral configuration. With this classical system, generating such effects requires rigorous experimental environments which makes their practical applications difficult [36]. Thus, modern systems that are based on plasmonic nanostructures are designed to present such effects [37]. MIM WG, when coupled with some resonators, generates the FR effect [38], and EIT-like effect [39]. In EIT-like effect, two or more resonances at similar resonance frequencies with different spectral widths are coupled. These effects are governed by SPP modes and plasmonic structures which are described in the next section.

### 2.2. Fano sensors based on plasmonic structures

Fano sensors can be designed either by localized surface plasmon (LSP) modes (in case of nanoparticles) or SPPs modes [40]. However, SPPs modes are often used because these modes have larger association regions and a prolonged decay span in the adjoining media. Thus, the SPPs modes using Fano sensors are more susceptible to the adjacent mass media of gases, liquids, and macromolecular layers. They are generally realized in regular metallic layouts for ease of fabrication and suited experimental

sensing [40]. However, the ordered structures, due to their high packing density are not appropriate for highly integrated optical circuits. To overcome this problem, FRs have been recently implemented in ultra-compact plasmonic structures [41] which are best at generating SPP modes.

Similar to the FR effect, another equally important optical effect used to equip plasmonic sensors and more is the EIT effect. This effect is visualized when two modes (waveguide mode and SPP mode) are coupled to each other having the same resonance frequency which is distinguished by a sharp communication band in the middle of a broad absorption band [28]. EIT effect which is emerged by plasmonic architectures is frequently named plasmon-induced transparency (PIT) [10]. Structures based on the MIM technology producing these effects may be potentially used in sensing applications because they provide sharp resonances. As compared to the conventional surface plasmon resonance (SPR) sensors, the FR-based sensors can roughly enhance the sensing *S* by two folds of magnitude [42]. Moreover, opposite to the Lorentzian resonance, the FR shows a unique sharp and uneven line profile, and this peculiar feature of the FR guarantees its implementations in sensors [14], switches [43], wavelength demultiplexing [44], and more. Recently, multiple FRs emerging architectures have drawn much attention because they can be used for multitasking like biochemical sensing, spectroscopy, and multicolour nonlinear processes [45] in a parallel matter. Moreover, the steep dispersion of the FR profile is very useful for several applications including sensors, lasing, switching, nonlinear, and slow-light devices [14,46–50]. The spectral lines due to the Fano effect are more tapered than the regular Lorentzian line shape, thereby replacing the Lorentzian resonance-based sensor and proving themselves as a promising solution for sensing applications [15]. Moreover, the tapered nature of Fano peaks/dips ensures achieving the high *S* and the ultra-high FoM that are needed for sensing applications.

Researches on the coupled MIM WG system generating FRs use existing numerical methods like transmission line theory [51], scattering theory [52], and coupled-mode theory (CMT) [53]. Among them, the CMT-based transfer matrix method (TMM) is widely used for the spectral analysis of the FR-based MIM WG-resonator system w here MIM WG-resonator occasionally constructs the Fabry-Perot (FP)-like mechanism [28]. This method provides a better way to study the interaction between the resonators.

## 3. Materials and methods

### 3.1. Materials

FRs have been discovered in plasmonic nanoparticles such as Au and Ag. Furthermore, these metals are used in the construction of WG and WG-coupled structures as plasmonic materials.

Other commonly used materials in plasmonics are metallic alloys, metallic compounds, graphene, aluminium (Al), and noble metal [e.g., Copper (Cu)] showing better stability at room temperature [26]. They act as a source of free electron gas in a layered WG. Another distinctive property of MIM WG that has a significant impact on the Fano parameter is the metal layers ability to control

undesired scattering loss due to their rough surface [26]. The best way to choose the plasmonic metal is to see the low resistivity specified by the reactive part of the dielectric plot (which indicates an ohmic loss or DC conductivity), and the small imaginary part. In the near-infrared (NIR) frequency regime and visible frequency regime, Ag shows this feature offering the best conductivity, proving it as a highly favoured material. On the contrary, due to its easy oxidation, Au can be an option in this frequency ranges [54]. But, for generating the FRs in the visible range, Ag is preferred more than Au because most of the FR-based sensors which have used Au have Fano peaks in the NIR which are less practical for sensing applications [55]. Another way to select plasmonic metals is based on their ability to generate high-quality traveling SPPs at the insulator/metal interface. This feature is a simple result of the metal dielectric function (DF). The dielectric plots of metals Au, and Ag are shown in Figs. 5(a) and 5(b), respectively.
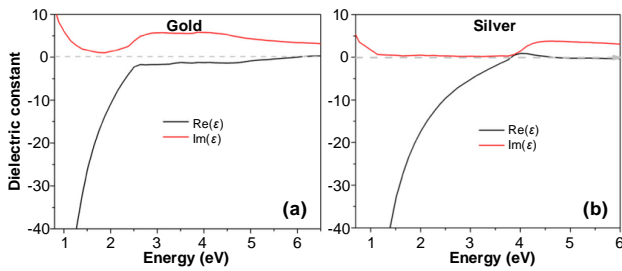


**Fig. 5.** Dielectric constants of gold (Au) (a) and silver (Ag) (b) [26].

According to Ag DF, the dielectric permittivity is a complex function that consists of a real part that signifies the polarization response, and the imaginary part gives the optical losses. DF also allows to investigate the fundamental excitations of free carriers and interband absorption, as well as the basic surface plasmon properties supported by Ag surface [56]. However, the abundant studies used the Drude model to represent the DF of Ag or Au, as it does not have to incorporate the interband transition in the near-mid infrared regime, but it accurately represents the optical response of Ag or Au [57]. Since Ag (or metals) have many free electrons, they provide the negative real permittivity that is required for any plasmonic materials. Of the two, Ag has been widely used because of its low absorption and power consumption [18]. Moreover, it is easy to fabricate with high etch selectivity [58]. The permittivity of Ag in a relative form has been characterized by Drude which clearly shows its frequency dependence. The relationship is defined as [48]:

$$\varepsilon_m(\omega) = \varepsilon_\infty - \frac{\omega_p^2}{\omega^2 + i\gamma\omega}.$$

(2)

This is popularly known as the Drude model. The symbols are defined as: $\varepsilon_\infty$ (= 3.7) is the dielectric constant when the angular frequency is infinite, $\omega_p$ (= 9.1 eV) is the mass plasma frequency, $\gamma$ (= 0.018 eV) is the electron collision frequency, and $\omega$ is the angular frequency of light in the air. For a long wavelength, however, this relation causes a large error. Thus, to carry the information of both absorption losses due to interband transition and

frequency-dependent scattering phenomenon, the Ag permittivity can be expressed by the Lorentz dispersion representation as [59]:

$$\varepsilon_m(\omega) = \varepsilon + \sum_{i=0}^{N} \frac{\omega_{p,i}^2}{\omega_{a,i}^2 - \omega^2 - i\omega_{c,i}\omega} ,$$

(3)

where $N$ is the number of oscillations with $\omega_i$ frequency. $\omega_a$ and $\omega_b$ are the Drude frequency and the Lorentzian frequency, respectively. The latter one arises from interband transition. Unfortunately, the calculation according to Eq. (3) is more complicated. Another revised Drude model to represent the polar nature of the metal which is widely used to calculate the dielectric constant of the valuable metals is the Debye model. The frequency-dependent permittivity of Ag as designated by the Debye-Drude model is expressed as [60]:

$$\varepsilon(\omega) = \varepsilon_\infty + \frac{\varepsilon_s - \varepsilon_\infty}{1 + i\omega\tau} + \frac{\sigma}{i\omega\varepsilon_0},$$

(4)

where $\varepsilon_\infty$ = 3.8344 is the permittivity at infinite frequency, $\varepsilon_s$ = −9530.5 is the unvarying permittivity, $\sigma$ = 1.1486 × 10^7 S/m is the conductivity, and $\tau$ = 7.35 s is the relaxation time.

For the theoretical study, either of the three models can be used. The MIM WG width is chosen sufficiently small as compared to the wavelength of the light ensuring the propagation of only fundamental mode inside it. The dispersion relation of the transverse magnetic (TM) fundamental modes in the MIM structure can be expressed as [61]:

$$\varepsilon_i k_2 + \varepsilon_m k_1 \coth\left(-\frac{ik_1\omega}{2}\right) = 0 ,$$

(5)

where $k_{1,2}^2 = \varepsilon_{i,m} k_0^2 - (k_0 Re(n_{\text{eff}}))^2$ is the transverse propagation constant in the air or the silver, $\omega$ is the MIM WG thickness, $k_0 = 2\pi/\lambda$ is the free space wave-vector, $Re(n_{\text{eff}})$ is the real part of an effective index, $\varepsilon_i$ and $\varepsilon_m$ are the dielectric constants of air and Ag, respectively. Even though Ag (or other metals) are used as a cladding layer in a plasmonic MIM WG, they are an inherent property of ohmic losses. Therefore, it is necessary to propose other materials to develop the robust plasmonic waveguides and devices [62]. One of the options is to adopt metallic alloys as plasmonic materials so that they help to shift the interband transition to other parts of the spectrum (not used for particular applications). For instance, noble-transition metal alloys (doping of bivalent transition metals cadmium and zinc to the monovalent noble metal) will add an extra electron to the electron pool which ultimately raises the Fermi level, thus, changing the optical spectra of the alloy [63]. Next, metallic compounds like aluminium-doped zinc oxide, gallium-doped zinc oxide, and indium-tin oxide demonstrate an extremely low built-in loss in the near-infrared regime. Similarly, nitrides of titanium and zirconium show strong CMOS compatibility for fabrication in the visible frequency band. In short, this category of plasmonic material replaces the metals both in the visible and near-infrared regimes by offering advantages like low inherent loss, semiconductor-based design with CMOS

compatibility and tunability [62]. Another popular plasmonic material is graphene. It is a 2D material that excites the SPs as that of metal/insulator interface. Inherently, it offers low loss due to interband transition in terahertz applications, but this loss is comparable to the noble metal in the infrared (IR) and visible (VIS) frequency ranges [63]. Dielectric material to be used as an insulator layer may be air (having RI=1.0) or silicon (having RI=3.5). Now, the MIM coupled structures based on SPP that create FRs are to be discussed because they play a vital role in generating the light-matter interaction and affect the FR modes behaviours.

### 3.2. The geometry of the Fano resonators

Plasmonic microresonators are of considerable interest for device designs and numerous of these architectures involve conjoining one or more cavities to a WG. Such MIM WG- resonator systems [34] can, of course, show Fano effects with sharp asymmetric line shapes, and they can be used for sensing. The resonance peaks can be shifted by changing the ambient RI by placing the substances to be sensed. In general, two ports FR-based sensors relied on the WG-resonator coupling can be provided in two ways, as shown in Figs. 6(a) and 6(b), respectively. The first method relied on a simple coupling geometry and the second configuration was a WG side-coupled to an individual or multiple mode cavity or multiple cavities. Based on this basic structure, the possibility to model an FR is to fix the geometry of a given system in such a way that two or more scattering paths are available. Specifically, the basic geometry can be upgraded by placing partially reflecting element(s) into the WG, by adjusting a coupling element
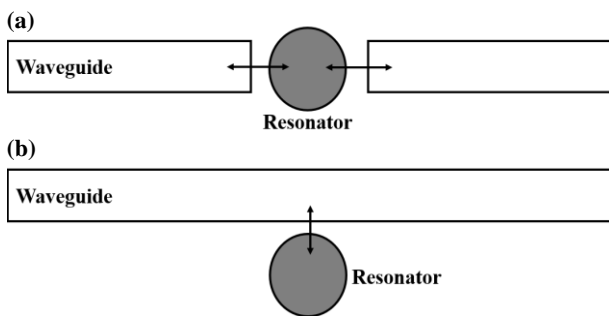


**Fig. 6.** Diagrammatic organization for a WG simple-coupled to a resonator (a), and a WG side-coupled to a resonator (b) [34].

through which the two WGs interact (support a localized mode) by making a mechanism of overlapping resonances and by coupling interferences. In this section, the focus will be on the creation of FR(s) by resonators with different geometrical shapes and with different structural parameters. From the literature, it can be stated that the resonators providing a continuum mode mainly include stub(s) [64], cavity [50], ring [65,66], rectangle [67,68], disk [69], circular ring [70], square [71], various resonators with defects [60,72], and their composite [73,74]. The resonators providing the localized mode mainly include the stub MIM WG [75], single baffle MIM WG, and double baffle MIM WG [76]. Further, making the appropriate defects on a WG or a resonator cavity gives a huge chance for appearance of the FR. Depending upon the resonator

architecture, the theories governing obtaining resonances are different and these resonances, when coupled with each other, generate FRs which are described in the following sections.

### 3.3. Theory of resonance due to a stub

The width of MIM WG and stub(s) are chosen to have an efficient power relay. The WG-stub system is shown in Fig. 7. The incident TM wave feeds the SPP mode in the WG which travels across the interface between the insulator and metal layers and allows a decaying signal to be evanescently linked to a stub that acts as a resonator showing resonance determined by the minimum transmission value at a particular wavelength known as the resonant wavelength. For the resonance to occur, the following condition needs to be met [48]:

$$2kRe(n_{\text{eff}})L + \varphi_r = 2m\pi, \quad m = 1, 2, 3, \dots, \quad (6)$$

where $k = \frac{2\pi}{\lambda}$ is the wave vector in the vacuum, $\varphi_r$ is the phase switch of the light reflected from the metal boundary of the insulator close to the stub, $m$ is the resonance order, $L$ is the stub effective length, and $Re(n_{\text{eff}})$ is the real part of the effective RI.
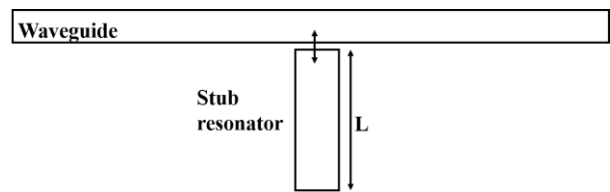


**Fig. 7.** Schematic of a WG side-coupled to the stub resonator.

However, this resonance has a broad spectrum. Once this arrangement is coupled with a circular cavity that generates the narrow discrete spectrum, the overall effect will mix these two spectra so that the Fano peak is generated [77]. The symmetry of the spectrum obtained from the WG-stub system can also be broken by inserting a nano-split in the stub in the calculated position [48].

### 3.4. Theory of resonance due to a rectangular cavity

Let us consider a rectangular cavity coupled with an MIM WG having the length $L$ as shown in Fig. 8.
Then, in a rectangular resonator, the SPPs phase shift occurs for each round trip. The gathered phase switch per complete journey for SPPs is $\emptyset = \frac{4\pi n_{\text{eff}}}{\lambda} + 2\varphi$ [78]. Constructive interference occurs when $\emptyset = 2N\pi$ indicating the resonant condition at certain wavelength of light. The corresponding resonant wavelength is calculated as:
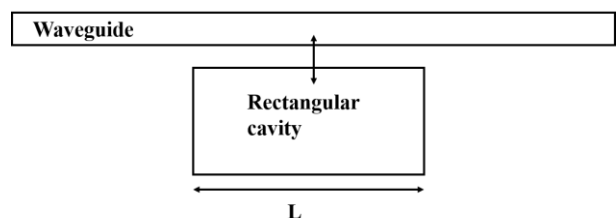


**Fig. 8.** Schematic of a WG side-coupled to a rectangular cavity.

$$\lambda = \frac{2n_{\text{eff}}L}{N - \varphi/\pi} \tag{7}$$

where $n_{\text{eff}}$ is the SPPs effective refractive index, $\varphi$ is the phase change by the SPP reflection away from the metal screen in the rectangular resonator, and $N$ is the resonance order in the rectangular cavity. The rate of change of the resonant wavelength with the variation of the effective length of the rectangle is given by the following relation:

$$\frac{d\lambda}{dL} = \frac{2n_{\text{eff}}}{N - \varphi/\pi} \, . \tag{8}$$

Since the geometric length of the plasmonic resonator and the wavelength of the light incident are related only to some order of magnitude of the wavelength, distinct conductor modes can be reflected TO and FROM the metal walls of the resonator establishing the FP resonator [50]. Thus, the WG modes have different field patterns and scattering characteristics showing resonances at different wavelengths in plasmonic resonators. The side-coupled cavity with a WG creates only a local discrete state. If the groove is connected to a WG on the next side, it will generate a continuum. If the entire system comes into the scene, it will mix these two spectra forming the FR [50].

### 3.5. Theory of resonance due to a square ring

In the MIM WGs, RI affects the guided modes obtained in Eq. (4). The layout of the WG resonator with a square ring is shown in Fig. 9.
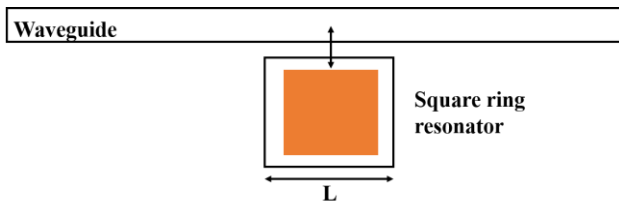


Fig. 9.  Schematic of a WG side-coupled to a square ring resonator.

Broad bright modes are obtained in the plasmonic MIM configuration. Also, narrow dark modes can be obtained using the WG-resonator structure. By coupling these two modes, FR is a built-in MIM square ring structure. The effective resonator length defines the wavelength of the resonant FR expressed in the following relation [79]:

$$\lambda_{\text{res}} = \frac{2n_{\text{eff}}L}{m - \Phi/2\pi}, \qquad m = 1, 2, 3, \dots \tag{9}$$

where $n_{\text{eff}}$, $m$, $L$, and $\Phi$ are the effective RI, resonance order, effective square length of the resonator, and SPP phase inversion, respectively.

### 3.6. Theory of resonance due to a discontinuity/break

Consider the gap "$g$" in the MIM waveguide as shown in Fig. 10 and our wish to observe the pattern of the light signal at the WG port to calculate the resonant wavelength.

Since the gap creates a discontinuity in the WG, it helps generate the resonances, which, in turn, cause multiple reflections between air and metal surfaces, and functions
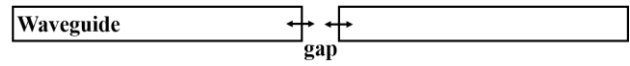


Fig. 10.  Schematic of a WG with a gap.

similar to the FP interferometer. Energy of the excited waves is stored by the gap because it acts as an energy storage unit and produces many barrier bands resulting in resonances at different wavelengths [66]. Multiple peaks are produced in transmission scattering under the resonance conditions governed by the following relationship:

$$2Re(\beta)g + 2\Phi = 2m\pi, \tag{10}$$

where $\beta$ is the propagation constant of SPPs.

Resonance wavelength of the FP cavity is calculated as:

$$\lambda_m = \frac{2n_{\text{eff}}g}{m - \frac{\varphi_r}{2\pi}}, \tag{11}$$

where integer $m = 0, 1, 2, 3, \dots$ and $\lambda_m$ is the resonant wavelength, $n_{\text{eff}}$ is the effective RI, and $\varphi_r$ is the phase reposition. Here, only a continuous broad band is observed and the transmission will disappear as the wavelength increases. Therefore, an additional resonator should be added to obey the principle of FR. One such resonator can be a circular edge nano cavity coupling with the WG and a baffle system providing a narrowband state. The entire system forms a Fano peak under resonance condition [70].

In addition, the transmittance of FP is set on by using the following relation:

$$T = \frac{(t)^2}{(1 - r^2) + 4r^2\sin^2(\varphi/2)}, \tag{12}$$

where $\varphi = 2\pi/\lambda \times 2g_{\text{eff}}$, $g_{\text{eff}}$ is the effective gap length which can be given as $g_{\text{eff}} = n \times n_{\text{eff}}$, $t$ and $r$ are the transmission and reflection ratios, respectively, and $\varphi$ is the metal absorption loss.

### 3.7. Theory of resonance due to a ring

Resonance is said to occur in a resonator which consists of a single ring when the light wave in the ring shows no phase change. An example of such a system has been shown in Fig. 11.
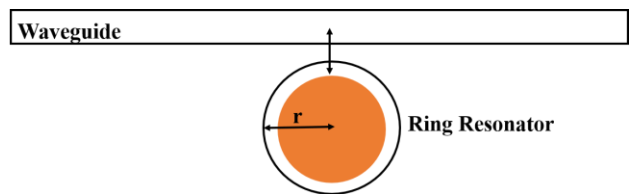


Fig. 11.  Schematic of a WG side-coupled to a ring resonator.

The condition for a co-phase can be noted as $\beta l = 2\pi m$, where $\beta$ is the phase constant and is given by $\beta = \frac{2\pi n_{eff}}{\lambda}$. This condition is called the resonant condition. The corresponding wavelength for the ring resonator is given by the relation [66]:

$$\lambda_{res} = \frac{2\pi r n_{eff}}{m},$$ (13)

where $m$ is the mode showing resonance (its value can be $m=1,2,3$), and $r$ is the radius of the ring. This structure only generates a discrete narrow state. To generate FR, the continuum state needs to be produced. A nanometallic wall inserted in the WG can fulfil this function. The structure created in this way blends these basic states to form the asymmetric Fano profile [80]. The transmission function of the ring is defined by the ratio of the output electric field ($E_{out}$) to the input electric field ($E_{in}$) and given by the following relation:

$$T = \frac{E_{out}}{E_{in}} = \frac{t - \alpha T_{hp} e^{-\beta d(l-l_{hp})}}{1 - \alpha T_{hp} e^{-\beta d(l-l_{hp})}},$$ (14)

where $t$ is the transmission coefficient between the ring and the WG, $l$ is the circumference of the resonator, $\alpha$ is the round-trip loss factor related to dielectric in the WG and the ring. The above-mentioned basic blocks generate the optical resonance which is dependent on many factors such as the physical dimensions of the device and the ambient RI. The relationship of the resonant wavelength in each block layout with the RI of the medium demonstrates their use as an RI sensor. The resonant relations defined by Eqs. (6), (7), (9), (11), and (13) show that there is a direct relationship between the resonant wavelength and RI (or redshift of wavelength with the RI). As mentioned, FRs arise due to the coupling of two counterparts. The Fano effect occurs only when the resonant state energy is in the range of the continuous state [81]. The amplitude of background scattering changes slowly with the energy change with the resonance energy, but the amplitude and phase of the resonant scattering change very quickly resulting in asymmetric linearity. In the saturated MIM WG-coupled structure above, a large linewidth resonance is typically excited to act as a continuous state, whereas a narrower linewidth resonance is usually excited to act as a discrete state. When their spectra have overlapped sections and their spatial positions are close enough, the near-field coupling can produce the FR. Furthermore, the loss of structural symmetry can cause the FR to be generated. Different plasmon resonances can be hybridized to each other by symmetry breaking, which allows the plasmon resonance with a large line width and the plasmon resonance with a narrow line width to be effectively linked to generate the FR [81]. Additionally, structural symmetry breaking enables the formation of plasmonic resonances as a result of the mutual coupling of similar nature which can generate two modes (modes with wide and narrow resonant line widths). These modes provide the continuous and discrete states, respectively. In the MIM WG-coupled system, two WG modes named symmetric and anti-symmetric modes could always be carried with no modal cut-off in the visible and near-infrared regimes [82]. The

gap can excite the anti-symmetric mode. Thus, in the broken plasmonic resonator, this small, trapped resonance interfered with the broad resonance based on the symmetric waveguide mode, resulting in the Fano resonance. Having this theoretical background, the MIM WG-resonator system generating the FRs is investigated through observing the Fano responses. The Fano response is frequently calculated using a coupled-mode theory (CMT), although the cavity mode amplitude and waveguide coupling loss are difficult to determine analytically.

### 3.8. Methods

Many kinds of literature have used analytical methods to study the transmission characteristics. CMT is a famous analytical method to analyse transmission characteristics. Some literature has used numerical methods for their studies like FEM and FDTD. For instance, a 2D FDTD method was adopted to examine the acts of the submitted shapes setting a perfectly matched layer (PML) absorbing boundary conditions [48,65,83–85] in their simulations. The optical responses of the designed structures were scrutinized by applying the finite difference method of commercially available COMSOL multi-physics in literature [35,60,61,86–88]. Some pieces of literature use only analytical methods for theoretical study whereas others adopt only numerical analysis methods for designing and manipulating the performances. Some cases have used both methods for the analysis of the transmission spectrum of FR-based sensors. Theoretical analysis of the MIM WG square convex ring resonator (SCRR) system, for example, is proposed in Ref. 61, where the Fano characteristics are examined using CMT. The following part is a description of the analytical procedure:

The structure consists of a metallic hinder in an MIM WG being co-phased with the SCRR shape. When the light enters the WG from its input port, SPPs are generated on the interface between the insulator layer and the metal. They carry information as energy within the core of MIM WG in the nano-sized architecture by surpassing the diffraction limit. The assumed parameters are: $1/\tau_0$ (inherent loss rate of SCRR), $1/\tau_e$ (the fading rate), and $K_1$ (the input linking amount of the propagation mode of WG). Then, the rate of change of normalized amplitude A with the time of the resonator is expressed as:

$$\frac{dA}{dt} = \left(j\omega_1 - 1/\tau_0 - 1/\tau_e\right)A + K_1(S_{1+} + S_{2+}) = j\omega A,$$ (15)

where $\omega$ is the incident light frequency, $\omega_1$ is the frequency at the resonance of SCRR, and $S_{1,2+}$ the amplitude of incoming light in the waveguide. If $S_{1,2-}$ represents the outgoing light amplitude of the WG, then based on the principle of energy preservation, the relation between energy going in and coming out of the WG can be shown as:

$$\begin{pmatrix} S_{1-} \\ S_{2-} \end{pmatrix} = C \begin{pmatrix} S_{1+} \\ S_{2+} \end{pmatrix} + K \begin{pmatrix} 0 \\ A \end{pmatrix},$$ (16)

where $C$ denotes the linking matrix between the entering waves and yielding waves through the metallic block which can be given as:

$$C = \begin{pmatrix} r & jt \\ jt & r \end{pmatrix}, \qquad (17)$$

The symbols are defined as: $r$ and $t$ are the reflection amplitude coefficient and the transmission amplitude coefficient, respectively, and $r^2 + t^2 = 1$. The coupling matrix denoted by $K$ between the output wave and the corresponding port has the relationship as follows:

$$K = \begin{pmatrix} 0 & K_1^* \\ 0 & -K_1^* \end{pmatrix}, \qquad (18)$$

where $K_1 = \sqrt{1/\tau_e}\, e^{j\theta}$ is the corresponding phase coupling coefficient. By using and manipulating Eqs. (15)–(18), and applying the principle of energy conservation and time-reversal symmetrical property, the transmission efficiency of the entire design can be estimated and expressed as the following equation:

$$T(\omega) = \left| \frac{S_{2-}}{S_{1+}} \right|^2 = \left| jt - \frac{1/\tau_e}{j(\omega - \omega_1) + 1/\tau_e + 1/\tau_0} \right|^2, \quad (19)$$

Similarly, the structure which comprises an MIM WG optically linked with rectangular and dual shunt-wound rings proposed in Ref. 87 has the transmittance $T$ which is expressed as:

$$T = \left| \frac{E_2}{E_1} \right|^2$$
$$= \left| \frac{K_1 K_2 [j(\omega - \omega_r) + K_r^2]}{[j(\omega - \omega_s) + K_1^2 + K_2^2 + K_r^2][j(\omega - \omega_r) + K_r^2] - K_r^2} \right|^2 \quad (20)$$

where $K_1$ and $K_2$ are the coupling coefficients between the input MIM WG and the rectangular cavity and between the output MIM WG and the rectangular cavity, respectively. $\omega$ is the light wave frequency, and $\omega_s$, $\omega_r$ are the resonance frequencies of the rectangular and ring cavities, respectively. The transmission spectrum to demonstrate both exhibiting the Lorentzian profile and the Fano line shape has been expressed based on the CMT method in Ref. 86 as:

$$T(\omega) = |t(\omega)|^2$$
$$= \left| t_B^2 + jt_B r_B - \frac{4/\tau}{j(\omega_0 - \omega) + 2/\tau_a + 4/\tau} \right|^2. \quad (21)$$

The FEM (or FDTD) tool is used to quantitatively simulate the sensor properties. The simulations results revealed that single or multiple Fano peaks can be generated depending upon the coupled-mode geometry which is narrow in width, asymmetric in nature with a strong field enhancement, and extremely sensitive to small variations in the resonator parameters and RIs of the slot. This feature enables the Fano effects to be used as RI sensors. Thus, it is interesting to evaluate the sensors based on the performance matrices by grouping the structures on a cavity or ring basis.

## 4. Comparative study of RI Fano sensors based on performance parameters: sensitivity and figure of merit

The most recent MIM WG-resonators as RI sensors exhibiting FR as single disk ring resonator (SDR), dual disk ring resonator (DDRR), rectangular cavity resonators, stubs resonators, groove resonators, slot cavities, symmetrical grooves resonators, square ring resonators (SRRs), split square ring resonators (SSRIs), T-shaped resonator, square convex ring resonator (SCRR), circular split-ring resonators (CSRRs), triangular stubs and split-ring resonators, M-type cavity with metallic baffle, and others are discussed here. The structures are either made upon the principles of direct-coupled resonator(s) or edge-coupled resonator(s).

### 4.1. Performance metrics

Mainly, the performance evaluating quantities of MIM Fano sensors are $S$ and FoM. To further rectify the executions of the sensors, the quality factor (Q-factor) is also evaluated. Q-factor is directly related to the ohmic losses. The lower the ohmic loss, the higher the Q-factor, and *vice versa* [89]. In many types of literature, however, Fano RI sensors are appraised based on $S$ and FoM, and these sensors are compared to their Lorentzian equivalents. These two factors serve as the foundation for validating the sensor performance regardless of the research methodology used (theoretical or empirical). Thus, their definitions and physical meanings are discussed as follows:

### 4.2. Sensitivity

It is the ratio of the change in shifting in the FR dip/peak with the possibly small change of RI [46]. Symbolically, $S = (\Delta\lambda_{res}) / \Delta n$ (nm/RIU) for RI sensors, where $\Delta\lambda_{res}$ is the change in a resonance wavelength brought about by the corresponding change in RIs. The reported figures of $S$ for a variety of MIM WG-resonator systems generating the Fano peaks have been reflected in Tables 1 through 3 in 2013−2021. The position of Fano dips/peaks can be varied by changing different design parameters which is described next. For example, the location of a Fano dip/peak and its profile are tuned by altering the length and the height of the cavity [46], respectively. The $S$ values have been found to vary depending upon the kind of assisting EM mode (decay length), resonant wavelength, agitation configuration, and underlayer properties [90]. Moreover, the structures with strong field confinement and low leaky loss are highly sensitive to change in the RI change [91]. Depending upon the geometry of the resonators, $S$ varies, for example, in the case of the MIM WG-ring resonator system generating the FRs, the dependency of $S$ has been reported in the literature (Table 2) where the samples of the same kind are filled. It has been proved that a sharp non-symmetrical line shape amplifies $S$ of the RI sensors [50,79,92–95]. Furthermore, the S increment can be obtained by using the concept of insertion of a metallic gap somewhere in the structure. Butt *et al.* proposed a square side of the ring resonator coupled to the main WG having metallic gaps placed diagonally on two opposite sides of the resonator. This arrangement has generated the FR. If the cavity is regularly

filled with nanodots, where a cluster of E-fields is excessive, it intensifies the SPPs at the boundary of nanodots, thus, enhancing the association between SPPs and the surrounding avenue. This ultimately increases $S$ and its maximum figure at the optimum size and the number of nanodots reaches up to 2464 nm/RIU [92] which is the highest $S$ reported in the case of FR-based MIM WG structures. From the definition of $S$, it is seen that its value can be increased either by keeping the change in RI fixed to some value and increasing the change in a resonant wavelength or by keeping change in RI as small as possible by keeping change in a resonant wavelength fixed to some value. But, for more RI-sensitive sensors, the change in RI should be as low as possible. $\Delta n \leq 0.01$ is used to detect gases, while $\Delta n \leq 0.02$ (or 0.025) is used to detect liquids. Only $S$ lacks to evaluate the total performance of the RI sensor because it cannot precisely define the optical resolution.

### 4.3. Figure of merit

FoM is a comprehensive parameter to judge plasmonic sensors. FoM measures the effect of a peak width on sensing performance. It is related to the optical resolution which is key to sensors. FoM, mathematically, is defined as FoM = $S$/FWHM (unitless), where FWHM is the full width at half maximum of the spectrum and $S$ is the sensitivity. FWHM is related to the mean lifetime of a surface plasmon (or propagation length). Moreover, it is related to the sharpness of the Fano peak. The more FWHMs, the lower the peak sharpness and *vice versa*. Therefore, in a way, it controls the sharpness of the peak. In some applications, at the fixed wavelength the change in light intensity is detected to calculate the matching FoM given by the relation FoM = $(\Delta T/\Delta n)/T$ [33], where $T$ is the transmittance and $\Delta T/\Delta n$ is the transmittance change at the fixed wavelength due to RI change. Some sensors detect a relative intensity change $(dI(\lambda))/(dn(\lambda))$ at the fixed wavelength $\lambda_0$. FoM in this case can be defined as

$$\text{FoM} = max \left| \frac{dI(\lambda)/dn(\lambda)}{I(\lambda)} \right| \text{ [46], where } \frac{dI(\lambda)}{dn(\lambda)} \text{ is the}$$

corresponding variation of intensity at a fixed wavelength caused by RI change. To increase the FoM, the peak sharpness should be high which is possible due to the coupling of different structures made of different materials with the main MIM WG, essentially, to achieve the FR. The values of FoM for a different plasmonic FR generating structures are summarized in Tables 1 to 3 which have adopted different approaches to lower the FWHM and increase the FoM. For instance, due to an extra sharp non-symmetric Fano line shape with extreme transmission at a resonance dip, the FoM of $3.2\times10^5$ is obtained in Ref. 33. Not only $S$ or FoM alone but $S$ and FoM both are generally used to analyse and differentiate divergent plasmonic sensors. This is because high FoM means high $S$ and high wavelength resolution. To facilitate a comparative study, the Fano sensors have been divided into three categories: cavity-based, ring-based, and composite. Cavity-based Fano sensors are compared in Table 1.

Table 1 shows that the cavity can be made up of a stub, groove, rectangle, square, U-shape, M-shape, and other shapes. However, these structures solo are unable to

Table 1.
Differentiation of Fano sensors based on the sensitivity ($S$), the figure of merit (FoM), and the cavity structure.

| Design structure | $S$ (nm/RIU) | FoM | Reference |
|---|---|---|---|
| MDM coupled with two grooves | 820 | $3.2\times10^5$ | [33] |
| MDM with stub and groove | 1260 | $2.3\times10^4$ | [35] |
| MDM coupled with closed rectangular cavity | 530 | 650 | [46] |
| MDM with two stubs filled with silver nano-split | 1060 | 176.7 | [48] |
| MDM and two identical slot cavities and rectangular cavities | 800 | $1.35\times10^4$ | [49] |
| MDM with groove and side-coupled with two cavities on one side | 1900 | $3.8\times10^4$ | [50] |
| MDM WG coupled with pair of cavities | … | $2.33\times10^4$ | [41] |
| MDM WG coupled with two stub cavities | … | 9673 | [64] |
| MDM WG coupled with double rectangular cavities | 596 | 7.5 | [67] |
| MDM side coupled with two asymmetric cavities in one side | … | 4800 | [83] |
| MDM WG coupled with two rectangular cavities | 985 | 54 | [85] |
| MDM with side-coupled cavity and a baffle | 1280 | … | [86] |
| MDM having a baffling side-coupled with cavities on each side | 1820 | $4.5\times10^4$ | [93] |
| MDM side coupled with two identical stubs resonators | $1.1\times10^3$ | $2\times10^5$ | [96] |
| MDM with two identical slot cavities and two symmetrical grooves | 903 | $3.1\times10^5$ | [97] |
| MDM with a disturbance side-linked with a square cavity | 1120 | $1.7\times10^5$ | [98] |
| MDM WG end coupled with slot cavity resonator | 1090 | $7.63\times10^4$ | [99] |
| MDM WG containing two gaps of $SiO_2$ coupled with two cavity resonators | 1010 | 29 | [100] |
| MDM WG with a metallic baffle and M-type cavities on either side | 760 | $1.56\times10^5$ | [101] |
| MDM WG with two baffles and a triangular groove cavity coupled with inverted U-shaped resonator | 840 | $3.9\times10^5$ | [102] |

produce Fano effects. The suitable combination between similar or dissimilar ones ensures structural symmetry breakage results in Fano interference. One of the methods

is to include nano-split(s) in the WG or cavity. A metallic baffle or a $SiO_2$ gap can be used to create a nano-split. Another option is to combine two or more conflicting structures by coupling the same structure multiple times, making it asymmetrical and mixing different structures (for example, mixing slot with groove, groove with groove, groove with stub, and groove with other shapes). There is a proper balance between groove and two-cavity system to get the best $S$ of 1900 nm/RIU and FoM of $3.8 \times 10^4$ [50]. The inverted U-shape resonator, as it forms an F-P cavity, causes an FR with a sharp dip and an asymmetrical line shape. The addition of a groove and metallic baffle creates an extra narrow dip (or narrower FWHM) resulting in the highest FoM of $3.9 \times 10^5$ [102]. As compared to other structures, the metallic baffles are difficult to fabricate due to the process technology. As a result, even though the insertion of metallic baffles achieves the antisymmetric mode needed for FR generation which ultimately ensures better sensing capabilities, the systems embedding baffle(s) are less preferred as far as the fabrication process is concerned. Such baffle-groove-cavity systems, on the other hand, have a very narrow FWHM that may be easily detected and tracked, enhancing sensing resolution significantly. In addition, if several FRs are wanted in the structures stated above, several cavities must be added to provide enough dark and bright modes, generating more Fano channels to obtain parallel sensing capability at the cost of a more complicated design. Ring-based Fano sensors are compared in Table 2.

Rings come in a variety of shapes, including the U-shape, square, circular, elliptical, and split versions of these shapes. When these geometries are either directly or indirectly connected to a bus WG, resonances are created that can be used in nano-sensing applications to detect RI fluctuations. These resonances, on the other hand, are the Lorentzian line forms. Therefore, it is necessary to install more structures to generate a discrete response, so that they interfere with each other and produce the Fano interference. Table 2 above shows examples of such combinations. The FR interference is induced by splitting resonance modes with varying coupling rates and resonance wavelengths, complying with the theoretical model mentioned in sections 3.5 and 3.7. The results of Table 2 also revealed the same. Fluctuations in the position of FR dips/peaks are caused by forms of a ring- (square and circular) and cavity- (tooth, stub, rectangle, and groove) coupling, as well as cavity-cavity phase, shifting, and RI of dielectric variations. As a result, these structures can be realized as nanosensors for detecting RI changes by using such flexible physical properties. Furthermore, in the ring resonator-based Fano sensors, the ring diameter plays a crucial role. If all the structural parameters are optimized, then the sensing performances are evaluated by quantifying FoM because it describes the link among the $S$, resolution and transmission. Since the Fano resonant dip/peak is sharp and the change in transmission at the resonant wavelength is quick, the FoM is ideal, resulting in the enhanced sensing performance. The findings demonstrate that the number of Fano peaks is substantially determined by the number of coupling loops surrounding the rings. Stub structures, on one hand, are basic and simple, yet they only produce a single FR. Ring structure, on the contrary, create many FRs despite their structural complexity. When the dielectric RIs

Table 2.
Differentiation of Fano sensors based on the sensitivity ($S$), the figure of merit (FoM), and the ring structure.

| Design structure | $S$ (nm/RIU) | FoM | Reference |
|---|---|---|---|
| Planner structure having nano-rods in U-shaped split ring resonator | 1380 | 52.1 | [15] |
| MDM WG with tooth cavity coupled with split ring cavity | 1200 | 122 | [60] |
| MDM WG coupled with square convex ring resonator with a baffle | 1120 | $2.68 \times 10^5$ | [61] |
| MDM WG side-coupled with concentric rings resonator | 1060 | 203.8 | [65] |
| MDM WG and a stub side-coupled with split ring resonator | $1.4 \times 10^3$ | $1.2 \times 10^5$ | [73] |
| MDM WG coupled with rectangular and ring resonator | 1125 | 75 | [74] |
| MDM WG containing two metallic baffles coupled to a ring resonator | 825 | $5.74 \times 10^4$ | [76] |
| Symmetrical MDM WGs coupled with a square ring resonator | 6400 | $1 \times 10^4$ | [79] |
| MDM WG with tangent rings | 880 | 964 | [84] |
| MDM WG with two triangular stubs coupled to split ring resonator | 1500 | 65.2 | [88] |
| MDM WG coupled with disk and ring cavity | 1100 | $2.73 \times 10^4$ | [103] |
| MDM WG with dual stubs side-linked ring resonator | 1000 | 4200 | [104] |
| MDM WG side-coupled with square ring resonator having nano-splits | 2464 | 259.8 | [92] |
| MDM with groove and ring resonator | 2000 | 8600 | [94] |
| MDM side-coupled with a rectangular ring loaded with a stub | 1000 | 992800 | [105] |
| MDM WG with an obstruct coupled with a circular split ring cavity | 1114.3 | 55.71 | [106] |
| MDM WG with two stubs coupled with a ring cavity | 2000 | $4.05 \times 10^4$ | [107] |

vary, so does the position of the FR. As a result, the resonant wavelength that we can detect will change. By sensing distinct resonant wavelengths, different RIs can be monitored. FR transmittance spectrum is also sharp, making it sensitive to changes in RIs. However, the adjustment of resonant wavelengths in a dynamic manner is limited. The symmetry of the entire ring structure is broken in the case of a split-ring resonator (SRR), resulting

in FR(s). The side-coupled circular-split ring resonance cavity sensor system can adjust the resonance more flexibly than the entire ring system. Since the various FRs are a collective effect of the system as a whole, tuning them precisely and independently is usually quite challenging. However, a disk-ring-stub-groove system can modulate these FRs semi-independently which is useful for RI sensing applications. Moreover, tuning of double FRs independently is made possible by changing the parameters of the stub cavities-ring cavity system. The groove-ring system allows tunability of dual Fano peaks in the near-infrared region. The $S$ of the system consisting of splits in the square ring with nano-dots embedded in the arms was increased to 2464 nm/RIU when compared to the standard square ring resonator system which had an $S$ of 1520 nm/RIU [92]. The square ring with nano-splits generates the FR, and the nano-dots boost the interaction of SPPs and dielectric medium in the ring. The concept of the dual stubs-ring cavity allows for the tunability of various FRs, resulting in a higher $S$ of 2000 nm/RIU and a FoM of $4.05 \times 10^4$ [107]. As the SRR based sensors are structurally simple, highly tunable, high sensing performer, and easily fabricable, they offer a lot of potential for use in nanosensors. From the results of Tables 1 and 2, it can be concluded that the resonating structures can substantially increase the $S$ and FoM. However, the issue to be addressed is to design such a structure that can generate multiple FRs with flexibly adjustable resonance wavelengths and fine turnability. The solution to address this problem is to adopt composite structures. Table 3 compares the composite Fano resonating structures used to detect the dielectric medium RI variations.

Various architectures are merged to generate the composite structure as shown in Table 3. The composite structures bring about multiple FR dips/peaks. For example, four FRs are generated via a composite system consisting of a stub-connected concentric rings-stub-ring. Due to their parallel processing capability, they are useful in multi-spectrum sensing applications which dominate in highly integrated photonic circuits. In addition, this system has an $S$ of 1600 nm/RIU and an FoM of $1.2 \times 10^6$ [113]. Thus, such a composite system has brought a proper balance in figures of two performance evaluating parameters ($S$ and FoM), which is the key criterion for plasmonic nanosensors.

The FR-based sensors presented here are theoretically studied and numerically validated through suitable simulating tools. The necessity is to experimentally validate these results and proceed with the process of the fabrication execution to make them commercially available as biochemicals sensing devices. Based on the conclusions of these tables, some recently developed FR-RI sensors and their evolution are surveyed next.

## 5. Some examples of recently developed Fano sensors

Having stated the basic blocks to generate FR and their sensing performance, it is worth adding the recent development trends and the way of generating the FR. Further, it is worth mentioning the individual blocks that contribute to FR achievements and the entire block to provide RI sensing features with a remarkable performance.

Table 3.
Differentiation of Fano sensors based on the sensitivity ($S$), the figure of merit (FoM), and the composite structure.

| Design structure | $S$ (nm/RIU) | FoM | Reference |
|---|---|---|---|
| MDM WG coupled with concentric ring and disk resonator | 640.6 | 287.9 | [108] |
| MDM WG end coupled with system of slot cavity and tooth-shape cavity and side-coupled semi-ring cavity | 1062 | 252.64 | [109] |
| MDM WG having dual symmetric rectangular stub linked to circular split-ring resonance cavity | 1180 | 5585.3 | [95] |
| MDM WG coupled with semi-ring rectangular composite cavity | 1260.5 | 1270.57 | [110] |
| Composite structure (circular, dual-side-coupled rectangular cavities and two MDM WGs) | ... | 8056 | [111] |
| MDM WG with dual identical rectangular stubs linked to elliptical ring resonator | 1550 | 43.05 | [112] |
| MDM WG stub-coupled with stub-coupled concentric rings on one side and ring on the other side | 1600 | $1.2 \times 10^6$ | [113] |

Starting from 2012 to present date, numerous MIM Fano resonator designs for RI sensing applications have been reported with the necessary investigation. 2-D schematics of some of such designs based on the ring structure from 2019 to 2021 are presented in Figs. 12(a)–12(j). Similarly, 2-D schematic views of the designs based on cavity resonators are presented in Figs. 13(a)−13(h). All designs have been constructed to justify the principle of coupling between WGs and resonators. The proper coupling between the WGs and resonators generates FRs. As the replacement of the material media (or change in effective RI) in the resonator causes the extreme change in the FRs, ultra-highly sensitive RI sensors have been proposed that exploit this optical effect. A structure composed of an MIM WG co-phased square convex ring resonator (SCRR) with a discontinuity where the baffle generates a broad steady-state and the SCRR forms a slender discontinuous state. As a result of coupling and interface between these two states, the FR occurs [61]. After the spectral analysis, the proposed sensor has achieved an $S$ of 1120 nm/RIU and an FoM of $2.68 \times 10^5$. Chen *et al*. proposed and investigated an RI sensor that relied on MIM WGs linked to dual rectangular cavities generating double FRs [85]. Yang *et al*. proposed an RI sensor including an MIM WG having two symmetrical triangles as stubs which coupled a circular ring cavity with a single split on it. The continuous broadband state results from the former structure and the discrete narrowband state from the latter structure, the interaction of these two states forms the FR [88]. The maximum $S$ and FoM achieved for this structure were
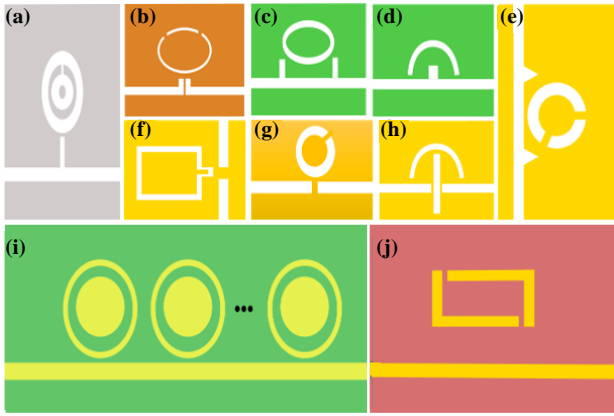
**Fig. 12.** Schematic setup for MIM WG ring resonators: side-coupled concentric rings and stubs [113] (a), symmetrical stubs-split elliptical ring resonator [95] (b), two stubs on MIM and side-coupled elliptical ring resonator [112] (c), stub semi-ring resonator [109] (d), triangular tooths and side-coupled split-ring resonator [88] (e), side-coupled square convex ring resonator [72] (f), side-coupled split-ring resonator and a stub [106] (g), edge-coupled cavity side-coupled with semi-ring resonator [110] (h), side-coupled cascaded ring resonators [108] (i), and side-coupled split-square ring resonator [92] (j).
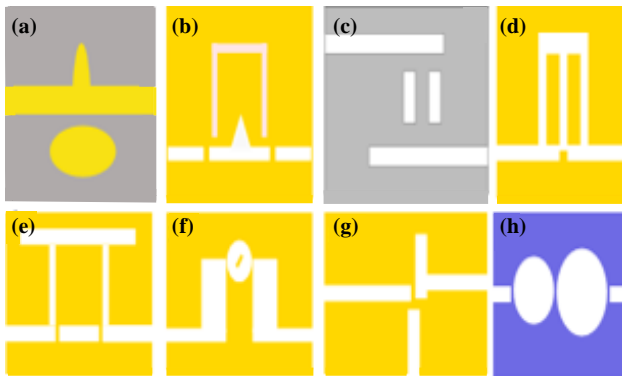


**Fig. 13.** Schematic setup for MIM plasmonic cavity designs published recently: side-coupled half-elliptical groove and elliptical cavity resonator [115] (a), inverted U-shaped resonator [102] (b), rectangular cavity resonators [116] (c), M-type cavity resonator [101] (d), a twin stub resonators rectangular cavity [118] (e), two rectangular cavities coupled by a circular cavity [111] (f), edge-coupled two rectangular cavities [85] (g), and edge-coupled asymmetric nano-disk resonators [9] (h).

1500 nm/RIU and 65.2, respectively. Fang *et al.* proposed a half-ring rectangular mixed cavity coupled with MIM WGs where there are four FRs having $S$ of 608.65 nm/RIU, 711.14 nm/RIU, 876.88 nm/RIU, and 1260.5 nm/RIU, and FoM*s* of 37.94 dB, 45.65 dB, 49.24 dB, and 41.67 dB, respectively [110]. Li *et al.* proposed MIM WGs end-linked vertical-cavity side-phase-matched by four cavities where seven Fano tips with asymmetrical line profiles are engineered which is very useful for parallel sensing applications [114]. Wang *et al.* demonstrated the MIM WG with a metallic discontinuity side-linked to a circular split-ring resonance hole which achieves a maximum $S$ of 1114.3 nm/RIU and an FoM of 55.71 after the analysis with FEM [106]. Qiao *et al.* proposed a sensor based on the MIM WG system with an M-kind cavity and an obstructed, which after simulations revealed an $S$ of 780 nm/RIU and an FoM as high as $1.56 \times 10^5$ [101]. All the above-stated

structures have used the concept of more light confinement inside the WG-resonators system to execute excessive sensing capability ($S$, FoM, etc.). The maximum light confinement has been made possible by improving their resonator make-up to boost the association of the incident light wave and the substance.

Another way to increase the light-matter interaction is to use the phenomenon of one-way propagation of reflection. With this purpose, Amoosoltani *et al.* has proposed dual asymmetric disk resonators end-linked to the both input and the output WG bus [9]. The calculated $S$ is of 1500 nm/RIU and FoM is of 242.66. Chen *et al.* developed an MIM type design which is formed from a CSRR cavity and a twin rectangular WG stubs, whereby FR is generated owing to the intervention between the wideband continuous state by the former structure and the narrowband discrete state by the latter structure [95]. Haffer *et al.* reported the MIM WG side-linked with a semi-elliptical trough on one side and an elliptical cavity on the other side, where FR modes are achieved due to these elements which may be used for RI sensing applications and slow light effect applications [115]. Su *et al.* demonstrated an RI sensor that is based on the MIM WG having dual stubs side-linked to an elliptical ring where the rectangular stub system constructed the Fabry–Perot cavity originating an FR having a maximum $S$ of 1550 nm/RIU [112]. Butt *et al.* introduced a new sensor structure based on a side-coupled square MIM WG ring resonator where a single nano-slot is obliquely positioned on different sides of the square housing. The hole is filled with Ag nano-dots to form an array. Due to nano-dots, the concentration of E - field in their vicinity is high which helps boost the SPPs at the boundary of the nano-dots which, again, enhances the light-matter interaction needed to enhance the $S$ and reach up to 2464 nm/RIU [92]. Hassen *et al.* proposed and demonstrated a plasmonic sensor made up of two MIM WGs side-coupled with two rectangular cavities forming two Fano peaks and achieving an $S$ of 886.16 nm/RIU [116]. Wang *et al.* put forward a coupled plasmonic system consisting of an MIM WG stub and ring resonators to implement the tetrad FRs and dual EIT reactions which together greatly enhances the refractive index $S$ to 1600 nm/RIU and FoM to $1.2 \times 10^6$ [113]. Wang *et al.* introduced a new sensor based on the sub-wavelength grating waveguide generating two modes: surface phonon polariton mode and Bloch mode which couple each other to create the FR [117]. Due to the strong light-matter interaction, the RI $S$ and FoM of the sensor go up to 7496 nm/RIU and 46432, respectively. Xiao *et al.* proposed a Fano sensor consisting of an inverted U-shaped resonant cavity and a triangular cavity to create the FRs which offer the best $S$ of 840 nm/RIU and the ultra-high FoM of $3.9 \times 10^5$ [102]. From the results, it is obvious that the edge-coupled resonators show relatively smaller FWHM as oppositely side-coupled designs. So, usually, edge-coupled systems are preferred in the FR generation, thereby, achieving higher FoM. Moreover, all these sensors have aimed at increasing the RI $S$ and FoM together. For the best performance of the sensor, their figures should be reached as high as possible. However, their fabrication should achieve similar performances in their commercialization. Therefore, fabrication as such is a great

challenge. More specifically, *S* also depends upon the environmental parameters and is quite critical to the method of fabrication, as well.

It can be observed from Tables 1, 2, and 3 and the survey of the modern cavity or ring resonator system (shown in Figs. 12 and 13) that the trend of the studies is heading towards multiple FRs-based sensors by modifying the present single FR-based sensors because they eventually make multi-spectrum sensing possible. Thus, a recent study trend is to obtain multiple FRs from a single composite structure to sense RI fluctuations, which wisely aids in regulating the FRs and achieving a good balance between the *S* and FoM. Now, it becomes worth mentioning the generation of FRs from the composite system and the modulation of these resonances by different means for the easier fabrication process.

## 6. Discussion

This section describes the tunability of FR-based RI sensors due to the variation of structural parameters, competing techniques with the Fano interference technique, their performance comparison, and prospects. FRs generating designs, as they provide high sensing outcomes and higher FoM (as seen from Tables 1, 2, and 3) are comparatively preferred in sensing applications. The FRs are brought about by the interaction of different waveforms generated by various arrangements of the plasmonic waveguide-resonator system. Moreover, they bring a proper balance between *S* and FoM. The structures mainly incorporated in this review are plasmonic waveguide-cavity resonator, and plasmonic waveguide-ring resonator. The cavity may be in the form of a groove, stub, and rectangular shape. The rings may be square, circle, and elliptical. The recent structures are constructed by combining these resonators. The components of the WG-resonator system not only contribute to the generation of Fano dips/peaks, but also play a crucial role in manipulating them. At the point of their optimized condition, the outcomes of the sensors are considered the best. Half of the portion that is related to the generation of FRs has been done in the preceding section. The remaining next half concerned with the manipulation of FRs is needed to be discussed. The tunability of FRs that emerged from some of the peculiar structures is discussed as follows:

In the structure consisting of MIM WG and symmetrical rectangular cavity, the Fano effect is catalysed by the interference linking a local four-pole and a wide spectral line from the rectangular cavity. The position of FR and Fano lines is tuned by altering both the length and the height of the rectangular cavity [46]. An asymmetrical transmission profile with a sharp peak has been formed by introducing a plasmonic groove in the wide stopband of the stub in the plasmonic waveguide-stub system where the necessary tuning of the contour and the Fano deep wavelength can occur by altering the height and length of the groove, and the height of stub [35]. The plasmonic WG-cavity system that generates different WG modes acts as a strategy paving the state-of-the-art to bring in the FRs. For instance, the asymmetric mode was generated by the introduction of a small structural break in the WG-cavity system [119]. Another idea for acquiring FR in the WG-cavity system is the introduction of a metallic baffle, for example, manifold Fano dips are realized by coupling four resonator cavities with the WG [86]. A plasmonic waveguide slot and metallic nano-wall system generate FR and it is tuned by changing the height of slot, width of nano-wall, and the distance between the slot and the metallic nano-wall [59]. The plasmonic WG-ring and rectangular resonator system achieved the FR as a result of linking the narrow-band spectral response by the ring resonator to the broadband spectral response by the rectangular resonator which is mainly calibrated through the change of ring perimeter, height of the rectangular resonator, and refractive index of the materials [74]. Introduction of a groove and a stub cavity in the plasmonic ring resonator constructed multiple Fano peaks originating from different processes, for instance, interference between the trough and ring resonator and interference between the stub and groove resonator [94]. The Fano peaks, thus, can be independently adjusted by modifying the structural specifications. Plasmonic WG-rectangular-hole resonator system consisting of two rectangular cavities between input and output generates three FRs which are easily tuned by changing the lengths of the resonators [85]. The coupled waveguide-cavity structure that consists of dual rectangular cavities and a single circular cavity embedding the metalcore creates four FRs. They are formed by the interlinkage of narrow modes from the circular cavity to wide modes from rectangular cavities [111]. The FR modes can be regulated by shifting the orientation angle of the metalcore. Plasmonic WG-stub-rectangular cavity resonator system generates dual Fano peaks: first onr by the interaction between two resonances – a weaker one achieved in the stub resonator and a stronger one in the FP resonator resulted from two stub resonators and WG connection; second one is achieved as a result of interlinking of the narrow discontinuous resonance contributed by the rectangular resonator to the wider continuous dip provided by the stub resonators [118].

From the literature, it is seen that the plasmonic ring resonator is one of the dominant components in the WG-resonator system for RI detection that could be integrated as photonic circuits because of its distinctive specifications. The placement of nano-dots in the ring where there is a big mass of E-field can enhance the *S* up to 61% in comparison to the regular MIM WG designs [24]. The same concept with the variety of dimensions and numerals of nano-dots considerably influences FoM. The plasmonic rectangular stub and elliptical ring resonator system facilitate both the symmetrical Lorentzian resonance and the FR phenomenon and can simply and mainly be calibrated by changing the longer radius and width of the elliptical ring along with changing the height of MIM WG, coupling distance, and height of the rectangular stub [112]. The important feature of the system is that the rectangular stub can construct the FP cavity that eases the FR. A hybrid-coupled system that consists of a tooth-shaped cavity and three side-linked half-rings facilitates up to eight channels of FRs [109]. Plasmonic waveguide-stub-ring resonator system helps to realize optical effects like the Fano effect and EIT. The popular example is a coupled plasmonic resonator that consists of two concentric ring resonators being connected through a stub as proposed in Ref. 113. The resonator ultimately provides four-pole Fano effects and dual EIT-like effects

which can be best regulated for optical sensing by changing the structural parameters offering more flexibility for integration on other photonics circuits, as well. Only the EIT-like effect has been realized in the coupled resonator(s) system made on the MIM WG platform. Such response, for example, is the result of a constructive interference between the nano-disk and stub-detuned resonator of the system consisting of a stub and a nano-disk on two sides of the MIM WG. The combined system acts as an RI sensor after the manipulation of the EIT effect showing an $S$ of 1200 nm/RIU, and FoM of $2.2 \times 10^4$ [120]. EIT-like transmission structure consisting of an MIM WG, two stub resonators, and a ring has shown an asymmetric line profile to act as an RI sensor with multiple EIT-like peaks. The maximum $S$ obtained is 1057 nm/RIU [121]. The EIT-like effect in a resonator system can be considered for radiative and non-radiative resonators that are directly or indirectly linked to the main WG. This effect in the plasmonic system is referred to as a PIT effect. This effect is the by-product of the phase and near-field coupling mechanisms. The key benefits of this effect are the broad bandwidth and the ability to manipulate at room temperature. The MIM WG side-coupling with two asymmetrical SRRs generate the PIT effect that can be manipulated to act as an RI sensor with an $S$ of 806 nm/RIU and an FoM of 66 [122]. A novel bowtie structure consisting of two detuned triangular resonators and an MIM WG generates the PIT effect which can be exploited to act as a PIT-based RI sensor. This sensor has a maximum $S$ of 1140 nm/RIU and a wavelength resolution of $8.8 \times 10^{-5}$ RIU. FoM$s$ for majority of EIT and PIT-based sensors are less compared with FR-based sensors. This shows that Fano line shape is much sharper and narrower than its counterparts EIT or PIT. As a result of this feature, FR is a good candidate for the sensitive detection.

The plasmonic triangular groove cavity and inverted U-like cavity system generate three sharp asymmetric Fano peaks which are regulated by height, width of the triangular groove cavity, coupling distance between the inverted U-shaped cavity, and triangular groove cavity, as well as height of the cavity which ultimately moderates the FoM of the structure [102]. A plasmonic hybrid system is composed of a double symmetric rectangular stub (DSRS) and a circular ring with metallic breaks resonance cavity where the FR occurred by the interference of the narrow-band discontinuous waveform excited by the CSRC and the wide-band continuous waveform excited by the DSRS [95]. The resonance wavelength in Fano effects is mainly regulated by the opening width of CSRRC, coupling distance of CSRRC and DSRSW, and width of the silver baffle in DSRSW. The ideal resonator to be used is a circular resonator. If its radius is too large, then the FWHM will grow and the sensing performance will suffer. The square straight waveguide is ideal for light transmission, but it will result in a bigger dimension at four right angles. The ellipse transmission loss can expand the sensing area, but its radius of curvature causes a significant material loss. Therefore, there is need to reach for another resonator that combines the advantages of these structures which is the racetrack ring resonator [123]. After examining the structures, it is seen that the composite systems, since they exploit the advantages of the constituent structures, showed the best performance despite their structural complexity.

As compared to dipolar resonances which are broad and symmetric profiles, FRs are sharp, narrow, and asymmetric profile resonances. Fano interference results in a sharp spectral peak. This peak (Fano peak) is extremely sensitive to changes in the environment. That is why it is used as a detection/sensing tool. Moreover, the FRs are quite scalable with the changes in device parameters and material media, their tunability is highly useful in diverse sensing applications. FRs have shown many promising features to be used as plasmonic sensors so that this area has received significant research interest. To name some of the important features: it has a rough line shape, tapered FWHM, strong field enhancement in a plasmonic field, and a high-quality factor [34]. The MIM WG system generating these resonances was treated as a replacement for the conventional Lorentzian system. FR is susceptible to changes in geometrical and environmental parameters. This tunability property makes it more suitable for sensors [31]. Due to the sharp line shape in FRs, $S$ and the FoM have shown improvement in the MIM WG-resonator system [48]. Compared to a single Fano resonance, a system with multiple Fano resonances not only has all the benefits listed above, but it can also modulate spectrum in many bands simultaneously which is more useful for multi-band sensor manufacturing. Also, the multiple FRs enable simultaneous sensing of the analytes. They have a wider range of operating wavelengths, thus, improving their flexibility. Moreover, those sensors that operate in the vicinity of telecommunication coverage are very important for connection to the communication system, for telemedicine and e-medicine. In short, they have high $S$ and response compared to other optical sensors.

In the above suggested Fano sensors and others, the continuum state mainly depends on the stub, groove, baffle of FP cavity structures while the discrete response is reinforced by the square, circle, ring, or nano-cavity. In these designs, more devotion is given to the impact of the nano-cavity on the FR profiles, and, comparatively, less attention is given to the effect of the continuum state. This gap is addressed in the case of structures based on Bragg where the periodic Bragg in the main WG can show the effect of the bandgap for the SPP waves. The system that consists of a Bragg grating bus WG and a side-coupled nano-cavity generates the FR due to the coupling of band edge modes of Bragg grating and resonant modes of nano-cavity. This system acts as an RI sensor with the best $S$ of 1425 nm/RIU and FoM of 1170 [124].

Since the metals (Ag or Au) used in making MIM WG are expensive, show extreme losses, limited working spectrum (ranges from visible to NIR wavelengths), and not suitable for the industry-mark manufacturing procedure, they have been replaced with different plasmonic material called titanium nitride (TiN). TiN-dielectric-TiN configuration-based composite structure made up of a groove and an SRR loaded with TiN dots because defects show the property of the RI sensor with $S$ and FoM of 1074.88 nm/RIU and 32.4, respectively [125]. This design has a manufacturing variation of 2.42% ensuring its reliability. Moreover, from the fabrication and working spectrum points of view, other plasmonic materials like graphene and metamaterials-based structures are expected to be used to generate the optical effects like FR or EIT and direct them to act as RI sensors [126,127].

# 7. Conclusions

Recent discoveries made in innovative optical effects such as EIT or FRs in plasmonic fields, as well as advances in simulation software to explore the field of plasmonic sensors based on these optical effects, have attracted more attention from researchers. Various plasmonic structures based on MIM WG have been introduced to implement the Lorentzian and FRs resonances and these features are used for sensing applications and more. This review mostly focused on SPP waveguides and FRs generating structures for refractive index sensing applications. Herein, various plasmonic Fano resonator designs were discussed that achieved sensitivities of 530 nm/RIU (the lowest one) and 2464 nm/RIU (the highest one). Fano sensors showed the ultra-high FoM, the key factor of the sensor, its minimum and maximum values reported were of 7.5 and $1.2 \times 10^6$, respectively. In general, FR-based sensors exhibit a trade-off between $S$ and FoM. Among the numerous WG-coupled structures like disk resonators, rectangular resonators, groove resonators, and ring resonators, the ring resonators were explored the most. With increasing remarkable findings on plasmonic waveguide-based sensors that operate under sub-wavelength regimes with greater accuracy and on-site detection, it is predicted that the branch of plasmonic Fano sensors will continue to drive the research and development of chip-based mixed lab technology. FR-based sensing is one of the key areas for further research and development due to its high performance as compared to other regular optical sensors. Furthermore, multi-FRs-based sensors will undoubtedly dominate soon the highly integrated circuit platform, due to their ability to detect different spectra. However, most sensors are designed and studied theoretically, so their implementation may be a challenge that needs to be addressed in the future.

## Authors' statement

All the authors have contributed equally to this review.

## References

[1] De Tommasi, E. *et al.* Frontiers of light manipulation in natural, metallic, and dielectric nanostructures. *Riv. del Nuovo Cim.* **44**, 1–68 (2021). https://doi.org/10.1007/s40766-021-00015-w

[2] Maier, S. Surface plasmon polaritons at metal /insulator interfaces. in *Plasmonics: Fundamentals and Applications:Chapter* 2, 1–2 (Springer, New York, 2007). https://doi.org/10.1007/0-387-37825-1_2

[3] Zhang, J., Zhang, L. & Xu, W. Surface plasmon polaritons: Physics and applications. *J. Phys. D. Appl. Phys.* **45**, 113001 (2012). https://doi.org/10.1088/0022-3727/45/11/113001

[4] Naik, G. V, Shalaev, V. M. & Boltasseva, A. Alternative plasmonic materials: beyond gold and silver. *Adv. Mater.* **25**, 3264–3294 (2013). https://doi.org/10.1002/adma.201205076

[5] Luo, X. & Yan, L. Surface plasmon polaritons and its applications. *IEEE Photon. J.* **4**, 590–595 (2012). https://doi.org/10.1109/JPHOT.2012.2189436.

[6] Saleh, B. E. A. & Teich, M. C. *Fundamentals of Photonics*. 1114–1115 (2$^{nd}$ ed.) (Wiley press, 2007). https://doi.org/10.1063/1.2809878

[7] Gramotnev, D. K. & Bozhevolnyi, S. I. Plasmonics beyond the diffraction limit. *Nat. Photonics* **4,** 83–91 (2010). https://doi.org/10.1038/nphoton.2009.282

[8] Kinsey, N., Ferrera, M., Shalaev, V. M. & Boltasseva, A. Examining nanophotonics for integrated hybrid systems: a review of plasmonic interconnects and modulators using traditional and alternative materials [Invited]. *J. Opt. Soc. Am. B* **32**, 121–142 (2015). https://doi.org/10.1364/JOSAB.32.000121

[9] Amoosoltani, N., Yasrebi, N., Farmani, A. & Zarifkar, A. A plasmonic nano-biosensor based on two consecutive disk resonators and unidirectional reflectionless propagation effect. *IEEE Sens. J.* **20**, 9097–9104 (2020). https://doi.org/10.1109/JSEN.2020.2987319

[10] Han, Z. & Bozhevolnyi, S. I. Radiation guiding with surface plasmon polaritons. *Reports Prog. Phys.* **76**, 016402 (2013). https://doi.org/10.1088/0034-4885/76/1/016402

[11] Lu, H., Wang, G. X. & Liu, X.M. Manipulation of light in MIM plasmonic waveguide systems. *Chin. Sci. Bull.* **58**, 3607–3616 (2013). https://doi.org/10.1007/s11434-013-5989-6

[12] Onbasli, M. C. & Okyay, A. K. Nanoantenna couplers for metal-insulator-metal waveguide interconnects. *Proc. SPIE* **7757**, 77573R (2010). https://doi.org/10.1117/12.876177

[13] Limonov, M. F., Rybin, M. V., Poddubny, A. N. & Kivshar, Y. S. Fano resonances in photonics. *Nat. Photonics* **11**, 543–554 (2017). https://doi.org/10.1038/nphoton.2017.142

[14] Luk'Yanchuk, B. *et al.* The Fano resonance in plasmonic nanostructures and metamaterials. *Nat. Mater.* **9**, 707–715 (2010). https://doi.org/10.1038/nmat2810

[15] Wang, J. *et al.* Double Fano resonances due to interplay of electric and magnetic plasmon modes in planar plasmonic structure with high sensing sensitivity. *Opt. Express* **21**, 2236–2244 (2013). https://doi.org/10.1364/OE.21.002236

[16] Lovera, A., Gallinet, B., Nordlander, P. & Martin, O. J. F. Mechanisms of Fano resonances in coupled plasmonic systems. *ACS Nano* **7**, 4527–4536 (2013). https://doi.org/10.1021/nn401175j

[17] Fan, J. A. *et al.* Fano-like interference in self-assembled plasmonic quadrumer clusters. *Nano Lett.* **10**, 4680–4685 (2010) . https://doi.org/10.1021/nl1029732

[18] Kazanskiy, N. L., Khonina, S. N. & Butt, M. A. Plasmonic sensors based on metal-insulator-metal waveguides for refractive index sensing applications: A brief review. *Phys. E Low Dimens. Syst. Nanostruct.* **117**, 113798 (2020). https://doi.org/10.1016/j.physe.2019.113798

[19] Verellen, N. *et al.* Mode parity-controlled Fano- and Lorentz-like line shapes arising in plasmonic nanorods. *Nano Lett.* 14, 2322–2329 (2014). https://doi.org/10.1021/nl404670x

[20] Huang, Y., Min, C., Dastmalchi, P. & Veronis, G. Slow-light enhanced subwavelength plasmonic waveguide refractive index sensors. *Opt. Express* **23**, 14922 (2015) . https://doi.org/10.1364/OE.23.014922

[21] Luo, S., Li, B., Xiong, D., Zuo, D. & Wang, X. A high performance plasmonic sensor based on metal-insulator-metal waveguide coupled with a double-cavity structure. *Plasmonics* **12**, 223–227 (2017). https://doi.org/10.1007/s11468-016-0253-y

[22] Rakhshani, M. R. & Mansouri-Birjandi, M. A. A high-sensitivity sensor based on three-dimensional metal–insulator–metal racetrack resonator and application for hemoglobin detection. *Photonics Nanostruct.* **32**, 28–34 (2018). https://doi.org/10.1016/j.photonics.2018.08.002

[23] Butt, M. A., Khonina, S. N. & Kazanskiy, N. L. Plasmonic refractive index sensor based on metal–insulator-metal waveguides with high sensitivity. *J. Mod. Opt.* **66**, 1038–1043 (2019). https://doi.org/10.1080/09500340.2019.1601272

[24] Butt, M. A., Khonina, S. N. & Kazanskiy, N. L. An array of nano-dots loaded MIM square ring resonator with enhanced sensitivity at NIR wavelength range. *Optik* **202**, 163655 (2020). https://doi.org/10.1016/j.ijleo.2019.163655

[25] Economou, E. N. Surface plasmons in thin films. *Phys. Rev.* **182**, 539–554 (1969). https://doi.org/10.1103/PhysRev.182.539

[26] Yang, R. & Lu, Z. Subwavelength plasmonic waveguides and plasmonic materials. *Int. J. Opt.* **2012** (2012). https://doi.org/10.1155/2012/258013

[27] Han, Z. & Bozhevolnyi, S. I. Plasmon-induced transparency with detuned ultracompact Fabry-Perot resonators in integrated plasmonic devices. *Opt. Express* **19**, 3251 (2011). https://doi.org/10.1364/OE.19.003251

[28] Zhan, S. *et al.* Slow light based on plasmon-induced transparency in dual-ring resonator-coupled MDM waveguide system. *J. Phys. D. Appl. Phys.* **47**, (2014). https://doi.org/10.1088/0022-3727/47/20/205101

[29] Piao, X., Yu, S., Koo, S., Lee, K. & Park, N. Fano-type spectral asymmetry and its control for plasmonic metal-insulator-metal stub structures. *Opt. Express* **19**, 10907–10912 (2011). https://doi.org/10.1364/OE.19.010907

[30] Fu, Y. H., Zhang, J. B., Yu, Y. F. & Luk'yanchuk, B. Generating and manipulating higher order Fano resonances in dual-disk. *ACS Nano* **6**, 5130–5137 (2012). https://doi.org/10.1021/nn3007898

[31] Fang, J., Zhang, M., Zhang, F. & Yu, H. Plasmonic sensor based on Fano resonance. *Guangdian Gongcheng/Opto-Electron. Eng.* **44**, 221–225 (2017). https://doi.org/10.3969/j.issn.1003-501X.2017.02.012

[32] Yu, Y. *et al.* Nonreciprocal transmission in a nonlinear photonic-crystal Fano structure with broken symmetry. *Laser Photonics Rev.* **9**, 241–247 (2015). https://doi.org/10.1002/lpor.201400207

[33] Chen, Z. & Yu, L. Multiple Fano resonances based on different waveguide modes in a symmetry breaking plasmonic system. *IEEE Photonics J.* **6**, 1–8 (2014). https://doi.org/10.1109/JPHOT.2014.2368779

[34] Miroshnichenko, A. E., Flach, S. & Kivshar, Y. S. Fano resonances in nanoscale structures. *Rev. Mod. Phys.* **82**, 2257–2298 (2010). https://doi.org/10.1103/RevModPhys.82.2257

[35] Chen, Z. *et al.* A refractive index nanosensor based on Fano resonance in the plasmonic waveguide system. *IEEE Photon. Technol. Lett.* **27**, 1695–1698 (2015). https://doi.org/10.1109/LPT.2015.2437850

[36] Wei, W., Yan, X., Shen, B. & Zhang, X. Plasmon-induced transparency in an asymmetric bowtie structure. *Nanoscale Res. Lett.* **14**, 246 (2019). https://doi.org/10.1186/s11671-019-3081-0

[37] Song, H., Singh, R., Cong, L. & Yang, H. Engineering the Fano resonance and electromagnetically induced transparency in near-field coupled bright and dark metamaterial. *J. Phys. D. Appl. Phys.* **48**, 035104 (2015). https://doi.org/10.1088/0022-3727/48/3/035104

[38] Yu, S., Piao, X., Hong, J. & Park, N. Progress toward high-Q perfect absorption : A Fano anti-laser. *Phys. Rev. A* **92**, 011802R (2015). https://doi.org/10.1103/PhysRevA.92.011802

[39] Yan, X. *et al.* High sensitivity nanoplasmonic sensor based on plasmon-induced transparency in a graphene nanoribbon waveguide coupled with detuned graphene square-nanoring resonators. *Plasmonics* **12**, 1449–1455 (2016). https://doi.org/10.1007/s11468-016-0405-0

[40] Chen, J., Gan, F., Wang, Y. & Li, G. Plasmonic sensing and modulation based on Fano resonances. *Adv. Opt. Mater.* **6**, 1701152 (2018). https://doi.org/10.1002/adom.201701152

[41] Deng, Y., Cao, G. & Yang, H. Tunable Fano resonance and high-sensitivity sensor with high figure of merit in plasmonic coupled cavities. *Photonics Nanostruct.* **28**, 45–51 (2018). https://doi.org/10.1016/j.photonics.2017.11.008

[42] Hayashi, S., Nesterenko, D. V. & Sekkat, Z. Fano resonance and plasmon-induced transparency in waveguide-coupled surface plasmon resonance sensors. *Appl. Phys. Express* **8**, 022201 (2015). https://doi.org/10.7567/apex.8.022201

[43] Heuck, M., Kristensen, P. T., Elesin, Y. & Mørk, J. Improved switching using Fano resonances in photonic crystal structures. *Opt. Lett.* **38**, 2466 (2013). https://doi.org/10.1364/OL.38.002466

[44] Chen, Z. *et al.* Plasmonic wavelength demultiplexers based on tunable Fano resonance in coupled-resonator systems. *Opt. Commun.* **320**, 6–11 (2014). https://doi.org/10.1016/j.optcom.2013.12.079

[45] Qi, J. *et al.* Independently tunable double Fano resonances in asymmetric MIM waveguide structure. *Opt. Express* **22**, 14688–14695 (2014). https://doi.org/10.1364/OE.22.014688

[46] Chen, Z.-Q. *et al.* Fano resonance based on multimode interference in symmetric plasmonic structures and its applications in plasmonic nanosensors. *Chin. Phys. Lett.* **30**, 057301 (2013). https://doi.org/10.1088/0256-307x/30/5/057301

[47] Gu, P., Birch, D. J. S. & Chen, Y. Dye-doped polystyrene-coated gold nanorods: Towards wavelength tuneable SPASER. *Methods Appl. Fluoresc.* **2**, 024004 (2014). https://doi.org/10.1088/2050-6120/2/2/024004

[48] Zafar, R. & Salim, M. Enhanced Figure of Merit in Fano resonance-based plasmonic refractive index sensor. *IEEE Sens. J.* **15**, 6313–6317 (2015). https://doi.org/10.1109/JSEN.2015.2455534

[49] Zhang, Y. *et al.* Evolution of Fano resonance based on symmetric/asymmetric plasmonic waveguide system and its application in nanosensor. *Opt. Commun.* **370**, 203–208 (2016). https://doi.org/10.1016/j.optcom.2016.03.001

[50] Zhang, Y. *et al.* Ultra-high Sensitivity plasmonic nanosensor based on multiple Fano resonance in the MDM side-coupled cavities. *Plasmonics* **12**, 1099–1105 (2017). https://doi.org/10.1007/s11468-016-0363-6

[51] Kocabas, S. E., Veronis, G., Miller, D. A. B. & Fan, S. Transmission line and equivalent circuit models for plasmonic waveguide components. *EEE J. Sel. Top. Quantum Electron.* **14**, 1462–1472 (2008). https://doi.org/10.1109/JSTQE.2008.924431

[52] Han, Z., Van, V., Herman, W. N. & Ho, P.-T. Aperture-coupled MIM plasmonic ring resonators with sub-diffraction modal volumes. *Opt. Express* **17**, 12678–12684 (2009). https://doi.org/10.1364/OE.17.012678

[53] Li, Q., Wang, T., Su, Y., Yan, M. & Qiu, M. Coupled mode theory analysis of mode-splitting in coupled cavity system. *Opt. Express* **18**, 8367 (2010). https://doi.org/10.1364/OE.18.008367

[54] Achanta, V.G. Surface waves at metal-dielectric interfaces: Material science perspective. *Rev. Phys.* **5**, 100041 (2020). https://doi.org/10.1016/j.revip.2020.100041

[55] Niu, L., Zhang, J. B., Fu, Y. H., Kulkarni, S. & Luky`anchuk, B. Fano resonance in dual-disk ring plasmonic nanostructures. *Opt. Express* **19**, 22974–22981 (2011). https://doi.org/10.1364/OE.19.022974

[56] Kolwas, K. & Derkachova, A. Impact of the Interband transitions in gold and silver on the dynamics of propagating and localized surface plasmons. *Nanomaterials* **10**, 1411 (2020). https://doi.org/10.3390/nano10071411

[57] Thomas, P. A. Plasmonics. in *Narrow Plasmon Resonances in Hybrid Systems* 7–27 (Springer, 2018). https://doi.org/10.1007/978-3-319-97526-9

[58] Noah, N. M. Design and synthesis of nanostructured materials for sensor applications. *J. Nanomater.* **2020**, 8855321 (2020). https://doi.org/10.1155/2020/8855321

[59] Chen, F. & Yao, D. Realizing of plasmon Fano resonance with a metal nanowall moving along MIM waveguide. *Opt. Commun.* **369**, 72–78 (2016). https://doi.org/10.1016/j.optcom.2016.02.024

[60] Zhang, Y. *et al.* High-sensitivity refractive index sensors based on Fano resonance in the plasmonic system of splitting ring cavity-coupled MIM waveguide with tooth cavity. *Appl. Phys. A* **125**, 13 (2019). https://doi.org/10.1007/s00339-018-2283-0

[61] Chen, Y., Xu, Y. & Cao, J. Fano resonance sensing characteristics of MIM waveguide coupled square convex ring resonator with metallic baffle. *Results Phys.* **14**, 102420 (2019). https://doi.org/10.1016/j.rinp.2019.102420

[62] Naik, G. V., Kim, J. & Boltasseva, A. Oxides and nitrides as alternative plasmonic materials in the optical range. *Opt. Mater. Express* **1**, 1090–1099 (2011). https://doi.org/10.1364/OME.1.001090

[63] West, P. R. *et al.* Searching for better plasmonic materials. *Laser Photonics Rev.* **4**, 795–808 (2010). https://doi.org/10.1002/lpor.200900055

[64] Deng, Y. *et al.* Tunable and high-sensitivity sensing based on Fano resonance with coupled plasmonic cavities. *Sci. Rep.* **7**, 10639 (2017). https://doi.org/10.1038/s41598-017-10626-1

[65] Zhang, Z. *et al.* Plasmonic refractive index sensor with high figure of merit based on concentric-rings resonator. *Sensors* **18**, 116 (2018). https://doi.org/10.3390/s18010116

[66] Chauhan, D., Adhikari, R., Saini, R. K., Chang, S. H. & Dwivedi, R. P. Subwavelength plasmonic liquid sensor using Fano resonance in a ring resonator structure. *Optik* **223**, 165545 (2020). https://doi.org/10.1016/j.ijleo.2020.165545

[67] Zhang, Z., Luo, L., Xue, C., Zhang, W. & Yan, S. Fano resonance based on metal-insulator-metal waveguide-coupled double rectangular cavities for plasmonic nanosensors. *Sensors* **16**, 22–24 (2016). https://doi.org/10.3390/s16050642

[68] Chen, Z., Cui, L., Song, X., Yu, L. & Xiao, J. High sensitivity plasmonic sensing based on Fano interference in a rectangular ring waveguide. *Opt. Commun.* **340**, 1–4 (2015). https://doi.org/10.1016/j.optcom.2014.11.081

[69] Tian, J., Wei, G., Yang, R. & Pei, W. Fano resonance and its application using a defective disk resonator coupled to an MDM plasmon waveguide with a nano-wall. *Optik* **208**, 164136 (2020). https://doi.org/10.1016/j.ijleo.2019.164136

[70] Chou Chao, C.-T., Chou Chau, Y.-F & Chiang, H.-P. Multiple Fano resonance modes in an ultra-compact plasmonic waveguide-cavity system for sensing applications. *Results Phys.* **27**, 104527 (2021). https://doi.org/10.1016/j.rinp.2021.104527

[71] Rakhshani, M. R. Optical refractive index sensor with two plasmonic double-square resonators for simultaneous sensing of human blood groups. *Photonics Nanostruct.* **39**, 100768 (2020). https://doi.org/10.1016/j.photonics.2020.100768

[72] Chen, Y., Xu, Y. & Cao, J. Fano resonance sensing characteristics of MIM waveguide coupled square convex ring resonator with metallic baffle. *Results Phys.* **14**, 102420 (2019). https://doi.org/10.1016/j.rinp.2019.102420

[73] Ren, X., Ren, K. & Cai, Y. Tunable compact nanosensor based on Fano resonance in a plasmonic waveguide system. *Appl. Opt.* **56**, H1–H9 (2017). https://doi.org/10.1364/AO.56.0000H1

[74] Tang, Y. *et al.* Refractive index sensor based on Fano resonances in metal-insulator-metal waveguides coupled with resonators. *Sensors* **17**, 784 (2017). https://doi.org/10.3390/s17040784

[75] Yang, X., Hua, E., Su, H., Guo, J. & Yan, S. A nanostructure with defect based on Fano resonance for application on refractive-index and temperature sensing. *Sensors* **20**, 4125 (2020). https://doi.org/10.3390/s20154125

[76] Chen, Y. *et al.* Sensing performance analysis on Fano resonance of metallic double-baffle contained MDM waveguide coupled ring resonator. *Opt. Laser Technol.* **101**, 273–278 (2018). https://doi.org/10.1016/j.optlastec.2017.11.022

[77] Binfeng, Y., Ruohu, Z., Guohua, H. & Yiping, C. Ultra-sharp Fano resonances induced by coupling between plasmonic stub and circular cavity resonators. *Plasmonics* **11**, 1157–1162 (2016). https://doi.org/10.1007/s11468-015-0154-5

[78] Zhang, Q., Huang, X.-G., Lin, X.-S., Tao, J. & Jin, X.-P. A subwavelength coupler-type MIM optical filter. *Opt. Express* **17**, 7549–7554(2009). https://doi.org/10.1364/OE.17.007549

[79] Rakhshani, M. R. Fano resonances based on plasmonic square resonator with high figure of merits and its application in glucose concentrations sensing. *Opt. Quantum Electron.* **51**, 287 (2019). https://doi.org/10.1007/s11082-019-2007-5

[80] Chen, F., Zhang, H., Sun, L., Li, J. & Yu, C. Temperature tunable Fano resonance based on ring resonator side coupled with a MIM waveguide. *Opt. Laser Technol.* **116**, 293–299 (2019). https://doi.org/10.1016/j.optlastec.2019.03.044

[81] He, Y. *et al.* Convert from Fano resonance to electromagnetically induced transparency effect using anti-symmetric H-typed metamaterial resonator. *Opt. Quantum Electron.* **52**, 391 (2020). https://doi.org/10.1007/s11082-020-02513-3

[82] Dionne, J. *et al.* A. Silicon-based plasmonics for on-chip photonics. *IEEE J. Sel. Top. Quantum Electron.* **16**, 295–306 (2010). https://doi.org/10.1109/JSTQE.2009.2034983

[83] Zhan, S. *et al.* Tunable nanoplasmonic sensor based on the asymmetric degree of Fano resonance in MDM waveguide. *Sci. Rep.* **6**, 22428 (2016). https://doi.org/10.1038/srep22428

[84] Guo, Z. *et al.* Plasmonic multichannel refractive index sensor based on subwavelength tangent-ring metal–insulator–metal waveguide. *Sensors* **18**, 1348 (2018). https://doi.org/10.3390/s18051348

[85] Chen, Y., Chen, L., Wen, K., Hu, Y. & Lin, W. Multiple Fano resonances in a coupled plasmonic resonator system. *J. Appl. Phys.* **126**, 083102 (2019). https://doi.org/10.1063/1.5105358

[86] Chen, Z., Song, X., Duan, G., Wang, L. & Yu, L. Multiple Fano resonances control in MIM side-coupled cavities systems. *IEEE Photonics J.* **7**, 1–10 (2015). https://doi.org/10.1109/JPHOT.2015.2433012

[87] Zhang, X. *et al.* Refractive Index Sensor based on Fano resonances in plasmonic waveguide with dual side-coupled ring resonators. *Photonic Sens.* **8**, 367–374 (2018). https://doi.org/10.1007/s13320-018-0509-6

[88] Yang, X. *et al.* Fano resonance in a MIM waveguide with two triangle stubs coupled with a split-ring nanocavity for sensing application. *Sensors* **19**, 4972 (2019). https://doi.org/10.3390/s19224972

[89] Wang, W.-D., Zheng, L. & Qi, J.-G. High Q-factor multiple Fano resonances for high-sensitivity sensing in all-dielectric nanocylinder dimer metamaterials. *Appl. Phys. Express* **12**, 075002 (2019). https://doi.org/10.7567/1882-0786/ab206a

[90] Špačková, B., Wrobel, P., Bocková, M. & Homola, J. Optical biosensors based on plasmonic nanostructures: a review. *Proc. IEEE* **104**, 2380–2408 (2016). https://doi.org/10.1109/JPROC.2016.2624340

[91] Li, S. *et al.* Fano resonances based on multimode and degenerate mode interference in plasmonic resonator system. *Opt. Express* **25**, 3525–3533 (2017). https://doi.org/10.1364/OE.25.003525

[92] Butt, M. A., Kazanskiy, N. L. & Khonina, S. N. Nanodots decorated asymmetric metal-insulator-metal waveguide resonator structure based on Fano resonances for refractive index sensing application. *Laser Phys.* **30**, (2020). https://doi.org/10.1088/1555-6611/ab9090

[93] Chen, Z., Cao, X. & Song, X. Side-coupled cavity-induced Fano resonance and its application in nanosensor. *Plasmonics* **11**, 307– 313 (2016). https://doi.org/10.1007/s11468-015-0035-y

[94] Wang, Y., Li, S., Zhang, Y. & Yu, L. Independently formed multiple Fano resonances for ultra-high sensitivity plasmonic nanosensor. *Plasmonics* **13**, 107–113 (2018). https://doi.org/10.1007/s11468-016-0489-6

[95] Chen, J. *et al.* Fano resonance in a MIM waveguide with double symmetric rectangular stubs and its sensing characteristics. *Opt. Commun.* **482**, 126563 (2021). https://doi.org/10.1016/j.optcom.2020.126563

[96] Chen, J. *et al.* Coupled-resonator-induced Fano resonances for plasmonic sensing with ultra-high figure of merits. *Plasmonics* **8**, 1627–1631 (2013). https://doi.org/10.1007/s11468-013-9580-4

[97] Wen, K. *et al.* Fano resonance with ultra-high figure of merits based on plasmonic metal-insulator-metal waveguide. *Plasmonics* **10**, 27–32 (2015). https://doi.org/10.1007/s11468-014-9772-6

[98] Yang, J. *et al.* Tunable multi-Fano resonances in MDM-based side-coupled resonator system and its application in nanosensor. *Plasmonics* **12**, 1665–1672 (2017). https://doi.org/10.1007/s11468-016-0432-x

[99] Wen, K., Chen, L., Zhou, J., Lei, L. & Fang, Y. A Plasmonic chip-scale refractive index sensor design based on multiple Fano reso-nances. *Sensors* **18**, 3181 (2018). https://doi.org/10.3390/s18103181

[100] Liu, Y. *et al.* Theoretical design of plasmonic refractive index sensor based on the fixed band detection. *IEEE J. Sel. Top. Quantum Electron.* **25**, 1–6 (2019). https://doi.org/10.1109/JSTQE.2018.2827661

[101] Qiao, L., Zhang, G., Wang, Z., Fan, G. & Yan, Y. Study on the Fano resonance of coupling M-type cavity based on surface plasmon polaritons. *Opt. Commun.* **433**, 144–149 (2019). https://doi.org/10.1016/j.optcom.2018.09.055

[102] Xiao, G. *et al.* High sensitivity plasmonic sensor based on Fano resonance with inverted u-shaped resonator. *Sensors* **21**, 1–12 (2021). https://doi.org/10.3390/s21041164

[103] Li, C. *et al.* Multiple Fano resonances based on plasmonic resonator system with end-coupled cavities for high-performance nanosensor. *IEEE Photonics J.* **9**, 1– 9 (2017). https://doi.org/10.1109/JPHOT.2017.2763781

[104] Shi, X. *et al.* Dual Fano resonance control and refractive index sensors based on a plasmonic waveguide-coupled resonator system. *Opt. Commun.* **427**, 326–330 (2018). https://doi.org/10.1016/j.optcom.2018.06.042

[105] Chen, Z. *et al.* Sensing characteristics based on Fano resonance in rectangular ring waveguide. *Opt. Commun.* **356**, 373–377 (2015). https://doi.org/10.1016/j.optcom.2015.08.020

[106] Wang, M., Zhang, M., Wang, Y., Zhao, R. & Yan, S. Fano resonance in an asymmetric MIM waveguide structure and its application in a refractive index nanosensor. *Sensors* **19**, 791 (2019). https://doi.org/10.3390/s19040791

[107] Yu, S., Zhao, T., Yu, J. & Pan, D. Tuning multiple fano resonances for on-chip sensors in a plasmonic system. *Sensors* **19**, 1559 (2019). https://doi.org/10.3390/s19071559

[108] Rahmatiyar, M., Danaie, M. & Afsahi, M. Employment of cascaded coupled resonators for resolution enhancement in plasmonic refractive index sensors. *Opt. Quantum Electron.* **52**, 153 (2020). https://doi.org/10.1007/s11082-020-02266-z

[109] Li, Z. *et al.* Manipulation of multiple Fano resonances based on a novel chip-scale MDM structure. *IEEE Access* **8**, 32914–32921 (2020). https://doi.org/10.1109/ACCESS.2020.2973417

[110] Fang, Y. *et al.* Multiple Fano resonances based on end-coupled semi-ring rectangular resonator. *IEEE Photon. J.* **11**, 1–8 (2019). https://doi.org/10.1109/JPHOT.2019.2914483

[111] Wang, Q., Ouyang, Z., Sun, Y., Lin, M. & Liu, Q. Linearly tunable Fano resonance modes in a plasmonic nanostructure with

a waveguide loaded with two rectangular cavities coupled by a circular cavity. *Nanomaterials* **9**, 678 (2019). https://doi.org/10.3390/nano9050678

[112] Su, H. *et al.* Sensing features of the Fano resonance in an MIM waveguide coupled with an elliptical ring resonant cavity. *Appl. Sci.* **10**, 5096 (2020). https://doi.org/10.3390/app10155096

[113] Wang, S., Zhao, T., Yu, S. & Ma, W. High-performance nano-sensing and slow-light applications based on tunable multiple Fano resonances and EIT-like effects in coupled plasmonic resonator system. *IEEE Access* **8**, 40599–40611 (2020). https://doi.org/10.1109/ACCESS.2020.2974491

[114] Li, Z. *et al.* Control of multiple Fano resonances based on a subwavelength MIM coupled cavities system. *IEEE Access* **7**, 59369–59375 (2019). https://doi.org/10.1109/ACCESS.2019.2914466

[115] El Haffar, R., Farkhsi, A. & Mahboub, O. Optical properties of MIM plasmonic waveguide with an elliptical cavity resonator. *Appl. Phys. A* **126**, 486 (2020). https://doi.org/10.1007/s00339-020-03660-w

[116] Hassan, M. F., Hasan, M. M., Ahmed, M. I. & Sagor, R.H. Numerical investigation of a plasmonic refractive index sensor based on rectangular MIM topology. in *2020 International Seminar on Intelligent Technology and its Applications ISITIA 2020*, 77–82 (IEEE, 2020). https://doi.org/10.1109/ISITIA49792.2020.9163755

[117] Wang, Y. *et al.* Design of sub wavelength-grating-coupled Fano resonance sensor in mid-infrared. *Plasmonics* **16**, 463–469 (2021). https://doi.org/10.1007/s11468-020-01313-5

[118] Chen, Y., Chen, L., Wen, K., Hu, Y. & Lin, W. Double Fano resonances based on different mechanisms in a MIM plasmonic system. *Photonics Nanostruct.* **36**, 100714 (2019). https://doi.org/10.1016/j.photonics.2019.100714

[119] Chen, Z., Chen, J., Yu, L. & Xiao, J. Sharp trapped resonances by exciting the anti-symmetric waveguide mode in a metal-insulator-metal resonator. *Plasmonics* **10**, 131–137 (2015). https://doi.org/10.1007/s11468-014-9786-0

[120] Pang, S. *et al.* The sensing characteristics based on electro-magnetically-induced transparency-like response in double-sided stub and a nano-disk waveguide system. *Mod. Phys. Lett. B* **31**, 1–9 (2017). https://doi.org/10.1142/S0217984917501019

[121] Zhang, Z. D. *et al.* Electromagnetically induced transparency and refractive index sensing for a plasmonic waveguide with a stub coupled ring resonator. *Plasmonics* **12**, 1007–1013 (2017). https://doi.org/10.1007/s11468-016-0352-9

[122] Akhavan, A., Ghafoorifard, H., Abdolhosseini, S. & Habibiyan, H. Metal-insulator-metal waveguide-coupled asymmetric resonators for sensing and slow light applications. *IET Optoelectron.* **12**, 220–227 (2018). https://doi.org/10.1049/iet-opt.2018.0028

[123] Shi, H. *et al.* A nanosensor based on a metal-insulator-metal bus waveguide with a stub coupled with a racetrack ring resonator. *Micromachines* **12**, 495 (2021). https://doi.org/10.3390/mi12050495

[124] Meng, Z.-M. & Qin, F. Realizing prominent Fano resonances in metal-insulator-metal plasmonic Bragg gratings side-coupled with plasmonic nanocavities. *Plasmonics* **13**, 2329–2336 (2018). https://doi.org/10.1007/s11468-018-0756-9

[125] Tathfif, I., Rashid, K. S., Yaseer, A. A. & Sagor, R. H. Alternative material titanium nitride based refractive index sensor embedded with defects: An emerging solution in sensing arena. *Results Phys.* **29**, 104795 (2021). https://doi.org/10.1016/j.rinp.2021.104795

[126] Li, Q. *et al.* Active control of asymmetric Fano resonances with graphene–silicon-integrated terahertz metamaterials. *Adv. Mater. Technol.* **5**, 1–7 (2020). https://doi.org/10.1002/admt.201900840

[127] Ge, J. *et al.* Tunable dual plasmon-induced transparency based on a monolayer graphene metamaterial and its terahertz sensing performance. *Opt. Express* **28**, 31781–31795 (2020). https://doi.org/10.1364/OE.405348